

Electronic Supporting Information

Heliconical smectic phases with transversal polar order

Mohamed Alaasar,^{a,b*} Marko Prehm,^a Maria-Gabriela Tamba,^c Nerea Sebastian,^c Alexey Eremin,^{c*} Yuri P. Panarin^d Jagdish K. Vij,^d Carsten Tschierske^{a*}

^a Department of Chemistry, Martin-Luther University Halle-Wittenberg, Kurt Mothes Str. 2, 06120 Halle (Saale), Germany

^b Department of Chemistry, Faculty of Science, Cairo University, 12613 Giza, Egypt

^c Department of Nonlinear Phenomena, Institute for Physics Otto von Guericke University Magdeburg, Magdeburg, Germany.

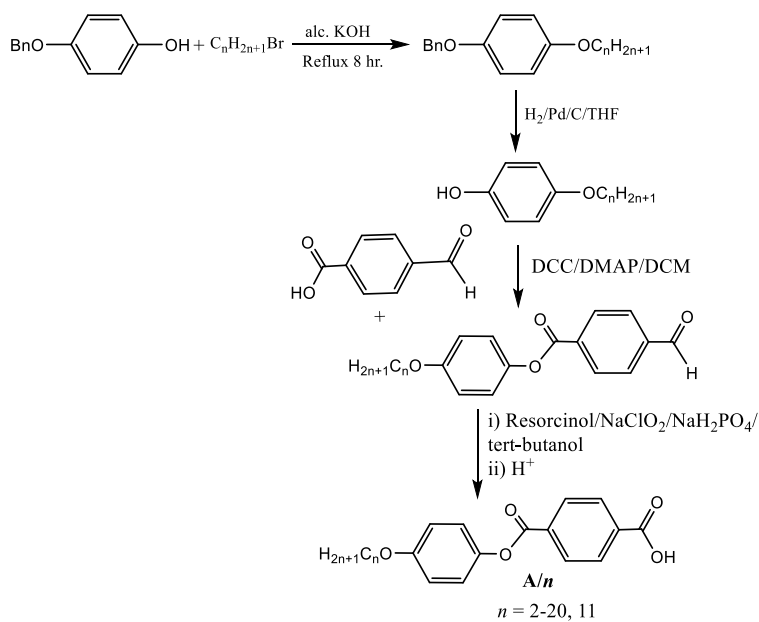
^d Department of Electronic and Electrical Engineering, Trinity College, Dublin, The University of Dublin, Dublin 2, Ireland

Contents

1. Synthesis and analytical data	S2
2. Investigation methods.....	S14
3. Additional DSC traces	S15
4. Additional XRD data	S16
5. Additional optical and electrooptic investigations	S31
6. Identification and confirmation of heliconical phases.....	S42
7. Additional SHG and dielectric data	S44
8. Additional Investigation of freely suspended films	S47
9. References	S48

1. Synthesis and analytical data

1-Bromoalkanes (Aldrich), 4-benzyloxyphenol (Aldrich), tert-butyl alcohol (Aldrich), sodium chlorite (Aldrich), sodium dihydrogenphosphate (Aldrich), potassium carbonate (Fluka), potassium hydroxide (Merck), 4-formylbenzoic acid (Aldrich), thionylchloride (Aldrich), 1,3-dicycloxycarbodiimide (DCC; Merck), 4-(*N,N*-dimethylamino)pyridine (DMAP) (Aldrich), 2,4-dihydroxybenzaldehyde (Aldrich) and hydroxylamine hydrochloride (Merck) were used as received without further purification. Chloroform (Merck) and dichloromethane (Merck) were dried separately over calcium chloride (Merck) and distilled before use. 2,4-dihydroxybenzonitrile was synthesized according to the procedure described in Ref.[S1] 4-(4-*n*-alkoxyphenyloxycarbonyl)benzoic acids were prepared according to reported standard procedures in Ref.[S2] The structure characterization of the synthesized bent-core compounds is based on ¹H-, ¹³C-NMR (Varian Unity 500 and Varian Unity 400 spectrometers, in CDCl₃ solutions, with tetramethylsilane as internal standard), MS [AMD 402 (electron impact, 70 eV)]. Microanalyses were performed using a Leco CHNS-932 elemental analyzer.



Scheme S1. Synthesis of 4-(4-*n*-alkoxyphenyloxycarbonyl)benzoic acids **A/n**.

1.1. Synthesis of 4-(4-*n*-alkoxyphenyloxycarbonyl)benzoic acids **A/n**

The synthetic route of the 4-substituted benzoic acids is shown in **Scheme 1** in a similar manner described by us before for 4-(4-*n*-hexyloxyphenyloxycarbonyl)benzoic acid and 4-(4-*n*-tetradecyloxyphenyloxycarbonyl)benzoic acid.[S2] As an example the ¹H-NMR obtained for

the intermediates compounds 4-eicosyloxy-1-benzyloxybenzene, 4-n-eicosyloxyphenol, 4-(4-n-eicosyloxybenzoyloxy)benzaldehyde and the acid 4-(4-n-eicosyloxybenzoyloxy)benzoic acid are given below. The remaining acids with $n = 2, 4, 6, 8, 10, 12, 14, 16$ and 18 are reported in references [S3], [S4], [S2b], [S5], [S6] and [S7], respectively.

1.1.1. 4-Eicosyloxy-1-benzyloxybenzene

$^1\text{H-NMR}$ (400 MHz, CDCl_3): δ 7.43–7.26 (m, 5H, Ar-H), 6.88 (d, 2H, Ar-H), 6.80 (d, 2H, Ar-H), 3.88 (t, $J = 6.6$ Hz, 2H, -OCH₂), 1.78–1.67 (m, 2H, -OCH₂CH₂), 1.53–1.16 (m, 34H, CH₂), 0.86 (t, $J = 6.9$ Hz, 3H, CH₃).

1.1.2. 4-n-Eicosyloxyphenol

$^1\text{H-NMR}$ (400 MHz, CDCl_3): δ 6.79–6.69 (m, 5H, Ar-H), 4.32 (s, 1H, Ar-OH), 3.87 (t, $J = 6.6$ Hz, 2H, -OCH₂), 1.78–1.67 (m, 2H, -OCH₂CH₂), 1.47–1.13 (m, 34H, CH₂), 0.86 (t, $J = 6.9$ Hz, 3H, CH₃).

1.1.2. 4-(4-n-Eicosyloxyphenyloxycarbonyl)benzaldehyde

$^1\text{H-NMR}$ (500 MHz, CDCl_3): δ 10.13 (s, 1H, Ar-CHO), 8.34 (d, $J = 8.2$ Hz, 2H, Ar-H), 8.00 (d, $J = 8.4$ Hz, 2H, Ar-H), 7.11 (d, 2H, Ar-H), 6.92 (d, 2H, Ar-H), 3.95 (t, $J = 8.2$ Hz, 2H, -OCH₂), 1.83–1.69 (m, 2H, -OCH₂CH₂), 1.56–1.10 (m, 34H, CH₂), 0.86 (t, $J = 7.0$ Hz, 3H, CH₃).

1.1.3. 4-(4-n-Eicosyloxyphenyloxycarbonyl)benzoic acid

$^1\text{H-NMR}$ (500 MHz, DMSO) δ 8.16 (d, $J = 8.6$ Hz, 1H, Ar-H), 8.08 (d, $J = 8.6$ Hz, 1H, Ar-H), 7.11 (d, $J = 8.8$ Hz, 1H, Ar-H), 6.91 (d, $J = 8.8$ Hz, 1H, Ar-H), 3.93 (t, $J = 8.3$ Hz, 2H, -OCH₂), 1.80–1.67 (m, 2H, -OCH₂CH₂), 1.46–1.02 (m, 34H, CH₂), 0.82 (t, $J = 6.9$ Hz, 3H, CH₃).

1.2. Synthesis of the bent-core mesogens 1/On

The synthetic route of the final bent core molecules is shown in Scheme 2. Similar to the method described for the homologues **1/O6**[S2b] and **1/O14**,[S2a] the corresponding 4-(4-n-alkoxyphenyloxycarbonyl)benzoic acid **A/n** (1 eq.) was refluxed in excess thionylchloride (SOCl_2) under argon atmosphere. After one hour the excess thionylchloride was removed under vacuum followed by the addition of 4-cyanoresorcinol (0.5 eq.), triethylamine (1.2 eq.) and few drops of pyridine (cat.) dissolved in anhydrous 15 mL CH_2Cl_2 /15 mL THF. The reaction mixture was refluxed with stirring for 6 hrs. At the end of the reaction as checked by TLC, the solution was cooled down to room temperature and poured into 10 mL of an aqueous solution

of 1 N HC1. The organic layer was extracted with dichloromethane and washed twice with saturated aqueous NaHC0₃ solution. The organic extracts were dried over anhydrous Na₂S0₄, filtered, and concentrated under vacuum. The crude solid materials were purified by column chromatography using CHCl₃ as eluent followed by twice recrystallization from ethanol/chloroform mixture. The analytical data obtained for final bent core materials are given below.

4-Cyano-1,3-phenylene bis[4-(4-n-ethyloxyphenyloxycarbonyl)benzoate], 1/O2:

Yield 67.33%, **¹H-NMR** (400 MHz, CDCl₃): δ 8.40–8.25 (m, 8H, Ar-H), 7.82 (d, J = 8.6 Hz, 2H, , Ar-H), 7.58 (d, J = 2.2 Hz, 2H, , Ar-H), 7.36 (dd, J = 8.6, 2.2 Hz, 2H, Ar-H), 7.13 (d, 4H, Ar-H), 6.93 (d, 4H, Ar-H), 4.04 (q, J = 7.0 Hz, 4H, -OCH₂), 1.42 (t, J = 7.0 Hz, 6H, CH₃). **¹³C-NMR** (100 MHz, CDCl₃): δ 164.39, 163.14, 162.81, 156.96, 156.92, 154.57, 153.25, 144.04, 144.00, 134.87, 134.75, 134.12, 132.54, 132.15, 130.64, 130.47, 130.42, 122.23, 122.20, 120.14, 117.26, 115.18, 115.19, 114.55, 104.51, 63.89, 14.82. **E. A.** Calc. for C₃₉H₂₉NO₁₀ C, 69.74; H, 4.35; N, 2.09. Found C, 69.70; H, 4.32; N, 2.12 %.

4-Cyano-1,3-phenylene bis[4-(4-n-butyloxyphenyloxycarbonyl)benzoate], 1/O4:

Yield 66.57%, **¹H-NMR** (400 MHz, CDCl₃): δ 8.40–8.24 (m, 4H, Ar-H), 7.82 (d, J = 8.6 Hz, 2H, Ar-H), 7.58 (d, J = 2.1 Hz, 1H, Ar-H), 7.36 (dd, J = 8.5, 2.2 Hz, 2H, Ar-H), 7.13 (dd, J = 9.0, 2.0 Hz, 2H, Ar-H), 6.94 (t, J = 6.3 Hz, 2H, Ar-H), 3.96 (t, J = 6.5 Hz, 2H, -OCH₂), 1.84–1.68 (m, 4H, -OCH₂CH₂), 1.56–1.41 (m, 4H, CH₂), 0.97 (t, J = 7.4 Hz, 6H, CH₃). **¹³C-NMR** (100 MHz, CDCl₃): δ 164.57, 163.30, 162.98, 157.34, 157.31, 154.73, 153.41, 144.14, 144.11, 135.04, 134.92, 134.29, 132.70, 132.30, 130.80, 130.63, 130.58, 122.36, 122.33, 120.30, 117.42, 115.35, 114.71, 104.67, 68.30, 31.46, 19.39, 13.99. **E. A.** Calc. for C₄₃H₃₇NO₁₀ C, 70.97; H, 5.12; N, 1.92. Found C, 70.93; H, 5.08; N, 1.96 %.

4-Cyano-1,3-phenylene bis[4-(4-n-decyloxyphenyloxycarbonyl)benzoate], 1/O10:

Yield 69.25%, **¹H-NMR** (400 MHz, CDCl₃): δ 8.41–8.24 (m, 8H, Ar-H), 7.82 (d, J = 8.6 Hz, 1H, Ar-H), 7.58 (d, J = 2.1 Hz, 1H, Ar-H), 7.37 (dd, J = 8.6, 2.2 Hz, 1H, Ar-H), 7.13 (d, J = 8.1 Hz, 4H, Ar-H), 6.93 (d, J = 8.0 Hz, 4H, Ar-H), 3.95 (t, J = 6.5 Hz, 4H, -OCH₂), 1.83–1.70 (m, 4H, -OCH₂CH₂), 1.56–1.14 (m, 14H, CH₂), 0.87 (t, J = 6.7 Hz, 6H, CH₃). **¹³C-NMR** (100 MHz, CDCl₃): δ 164.41, 163.17, 162.84, 157.20, 157.17, 154.56, 153.24, 144.97, 143.94, 134.76, 134.54, 134.12, 132.53, 132.19, 130.63, 130.47, 130.41, 122.19, 122.16, 120.18, 117.26, 115.22, 115.26, 110.02, 104.54, 68.47, 31.88, 30.89, 29.56, 29.37, 29.30, 29.25, 26.03,

22.66, 14.09. **E. A.** Calc. for **C₅₅H₆₁NO₁₀** C, 73.72; H, 6.86; N, 1.56. Found C, 73.47; H, 6.65; N, 1.55 %.

4-Cyano-1,3-phenylene bis[4-(4-n-undecyloxyphenyloxycarbonyl)benzoate], 1/O11:

Yield 66.97%, **¹H-NMR** (400 MHz, CDCl₃): δ 8.44–8.27 (m, 8H, Ar-H), 7.84 (d, J = 8.6 Hz, 1H, Ar-H), 7.60 (d, J = 2.2 Hz, 1H, Ar-H), 7.38 (dd, J = 8.5, 2.2 Hz, 1H, Ar-H), 7.15 (d, J = 8.2 Hz, 4H, Ar-H), 6.94 (d, J = 8.5 Hz, 4H, Ar-H), 3.97 (t, J = 6.5 Hz, 4H, -OCH₂), 1.85–1.73 (m, 4H, -OCH₂CH₂), 1.61–1.17 (m, 32H, CH₂), 0.89 (t, J = 7.0 Hz, 6H, CH₃). **¹³C-NMR** (126 MHz, CDCl₃): δ 164.39, 163.13, 162.79, 157.15, 157.13, 154.55, 153.23, 143.96, 143.92, 134.74, 134.11, 132.52, 132.12, 130.62, 130.46, 130.40, 122.18, 122.15, 120.12, 117.25, 115.18, 104.50, 68.47, 31.89, 29.59, 29.58, 29.56, 29.37, 29.31, 29.25, 26.02, 22.66, 14.09. **E. A.** Calc. for **C₅₇H₆₅NO₁₀** C, 74.08; H, 7.09; N, 1.52. Found C, 73.96; H, 6.94; N, 1.47 %.

4-Cyano-1,3-phenylene bis[4-(4-n-dodecyloxyphenyloxycarbonyl)benzoate], 1/O12:

Yield 68.99%, **¹H NMR** (600 MHz, CDCl₃): δ 8.43 – 8.30 (m, 8H, Ar-H), 7.84 (d, J = 8.6 Hz, 1H, Ar-H), 7.60 (d, J = 2.2 Hz, 1H, Ar-H), 7.38 (dd, J = 8.6, 2.2 Hz, 1H, Ar-H), 7.15 (d, J = 8.2 Hz, 4H, Ar-H), 6.94 (J = 8.5 Hz, 4H, Ar-H), 3.97 (t, J = 6.5 Hz, 4H, -OCH₂), 1.84 – 1.75 (m, 4H, -OCH₂CH₂), 1.52 – 1.20 (m, 36H, CH₂), 0.89 (t, J = 6.9 Hz, 6H, OCH₃). **¹³C-NMR** (126 MHz, CDCl₃): δ 164.40, 163.12, 162.80, 157.15, 157.13, 154.55, 153.23, 143.96, 143.92, 134.86, 134.74, 134.11, 132.52, 132.12, 130.62, 130.45, 130.40, 122.18, 122.15, 120.12, 117.24, 115.17, 104.49, 68.46, 31.89, 29.63, 29.61, 29.57, 29.55, 29.36, 29.32, 29.24, 26.01, 25.92, 22.66, 14.08. **E. A.** Calc. for **C₅₉H₆₉NO₁₀** C, 74.42; H, 7.30; N, 1.47. Found C, 74.37; H, 7.28; N, 1.44 %.

4-Cyano-1,3-phenylene bis[4-(4-n-hexadecyloxyphenyloxycarbonyl)benzoate], 1/O16:

Yield 70.01%, **¹H-NMR** (500 MHz, CDCl₃): δ 8.39–8.26 (m, 8H, Ar-H), 7.82 (d, J = 8.6 Hz, 1H, Ar-H), 7.58 (d, J = 2.1 Hz, 1H, Ar-H), 7.36 (dd, J = 8.6, 2.2 Hz, 1H, Ar-H), 7.13 (d, 4H, J = 9.3 Hz, Ar-H), 6.92 (d, J = 9.1 Hz, 4H, Ar-H), 3.95 (t, J = 6.5 Hz, 4H, -OCH₂), 1.83–1.72 (m, 4H, -OCH₂CH₂), 1.50–1.19 (m, 26H, CH₂), 0.86 (t, J = 6.9 Hz, 6H, CH₃). **¹³C-NMR** (100 MHz, CDCl₃): δ 164.42, 163.15, 162.82, 157.18, 157.15, 154.57, 153.26, 143.99, 143.95, 134.89, 134.77, 134.13, 132.55, 132.15, 130.64, 130.48, 130.42, 123.56, 122.20, 122.17, 120.15, 117.27, 115.19, 115.20, 114.55, 104.52, 69.68, 31.92, 30.90, 30.87, 29.69, 29.67, 29.65, 29.59, 29.58, 29.39, 29.35, 29.26, 26.04, 25.94, 22.68, 14.10. **E. A.** Calc. for **C₆₇H₈₅NO₁₀** C, 75.60; H, 8.05; N, 1.32. Found C, 75.65; H, 8.10; N, 1.28 %.

4-Cyano-1,3-phenylene bis[4-(4-n-octadecyloxyphenyloxycarbonyl)benzoate], 1/O18:

Yield 69.59%, **¹H-NMR** (400 MHz, CDCl₃): δ 8.44–8.24 (m, 8H, Ar-H), 7.82 (d, J = 8.6 Hz, 1H, Ar-H), 7.58 (d, J = 2.2 Hz, 1H, Ar-H), 7.36 (dd, J = 8.6, 2.2 Hz, 1H, Ar-H), 7.13 (d, 4H, J = 9.0 Hz, Ar-H), 6.93 (d, J = 9.1 Hz, 4H, Ar-H), 3.95 (t, J = 6.6 Hz, 4H, -OCH₂), 1.83–1.67 (m, 4H, -OCH₂CH₂), 1.55–1.16 (m, 30H, CH₂), 0.86 (t, J = 6.9 Hz, 6H, CH₃). **¹³C-NMR** (100 MHz, CDCl₃): δ 164.42, 163.15, 162.82, 157.18, 157.15, 154.58, 153.26, 143.99, 143.95, 134.89, 134.77, 134.13, 132.54, 132.15, 130.64, 130.48, 130.42, 123.56, 122.20, 122.17, 120.15, 117.27, 115.19, 115.20, 114.55, 104.53, 68.48, 31.92, 31.90, 30.90, 30.87, 29.69, 29.67, 29.65, 29.60, 29.58, 29.39, 29.35, 29.26, 26.04, 26.02, 25.94, 22.68, 14.10. **E. A.** Calc. for **C₇₁H₉₃NO₁₀** C, 76.11; H, 8.37; N, 1.25. Found C, 76.05; H, 8.28; N, 1.26 %.

4-Cyano-1,3-phenylene bis[4-(4-n-eicosyloxyphenyloxycarbonyl)benzoate], 1/O20:

Yield 64.35%, **¹H-NMR** (400 MHz, CDCl₃): δ 8.40–8.24 (m, 8H, Ar-H), 7.82 (d, J = 8.6 Hz, 1H, Ar-H), 7.58 (d, J = 2.2 Hz, 1H, Ar-H), 7.36 (dd, J = 8.6 Hz, J = 2.2 Hz, 1H, Ar-H), 7.12 (d, J = 8.0 Hz, 4H, Ar-H), 6.93 (d, J = 8.0 Hz, 4H, Ar-H), 3.95 (t, J = 6.5 Hz, 4H, -OCH₂), 1.83–1.72 (m, 4H, -OCH₂CH₂), 1.58–1.13 (m, 34H, CH₂), 0.86 (t, 6H, CH₃). **¹³C-NMR** (100 MHz, CDCl₃): δ 164.41, 163.15, 162.82, 157.18, 157.15, 154.57, 153.26, 143.99, 143.95, 134.89, 134.77, 134.13, 132.54, 132.15, 130.64, 130.48, 130.42, 123.56, 122.20, 122.17, 120.15, 117.27, 115.19, 115.20, 114.55, 104.52, 68.48, 31.92, 31.90, 30.56, 30.47, 30.90, 30.87, 29.69, 29.67, 29.65, 29.60, 29.58, 29.39, 29.35, 29.26, 26.04, 26.02, 25.94, 22.68, 14.10. **E. A.** Calc. for **C₇₅H₁₀₁NO₁₀** C, 76.56; H, 8.65; N, 1.19. Found C, 76.48; H, 8.64; N, 1.22 %.

1.3 Representative NMR spectra

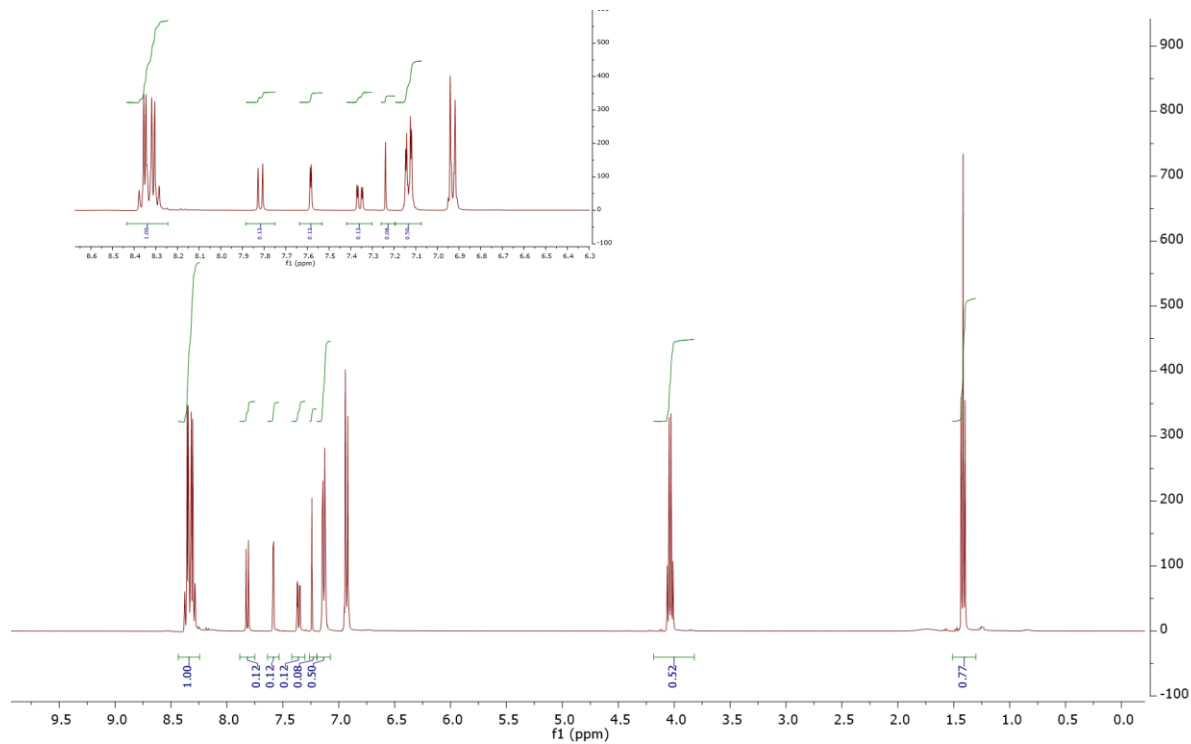


Figure S1a. ¹H-NMR spectrum (400 MHz, CDCl_3) of **1/O2**.

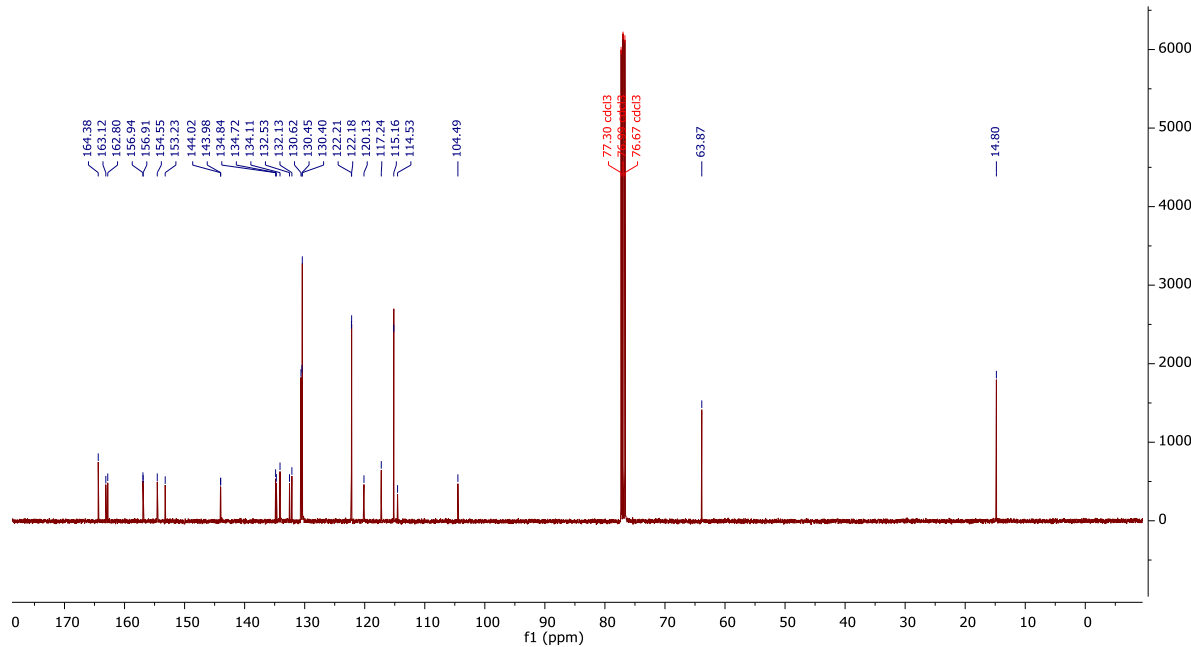
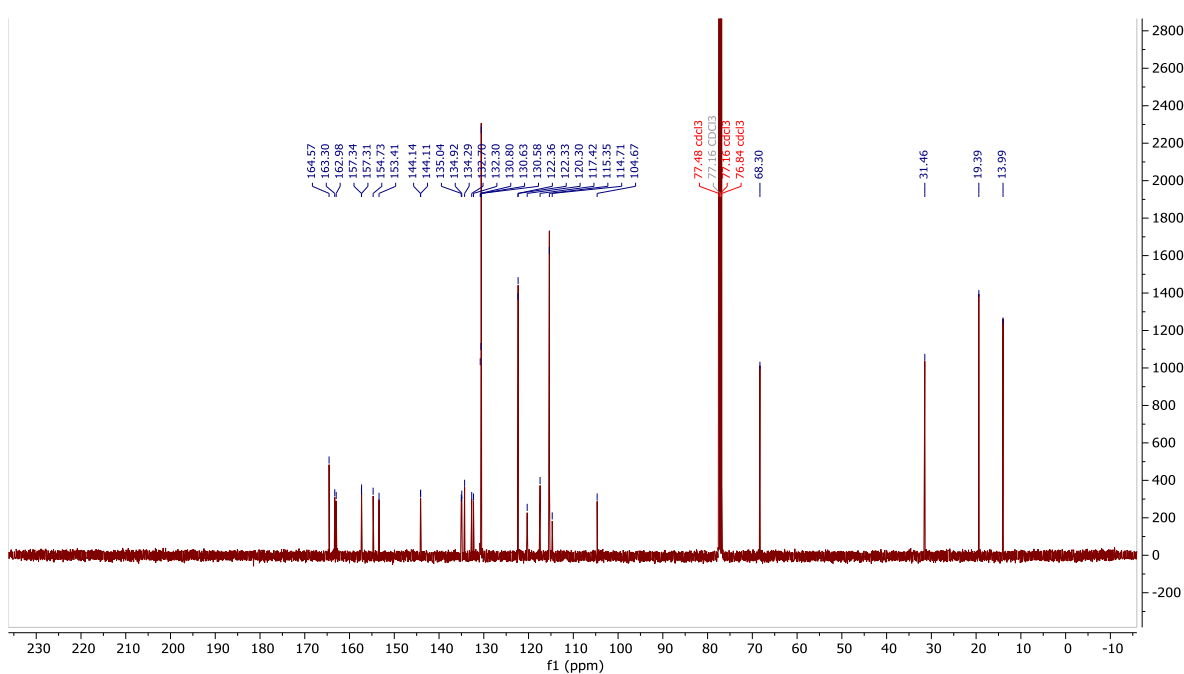
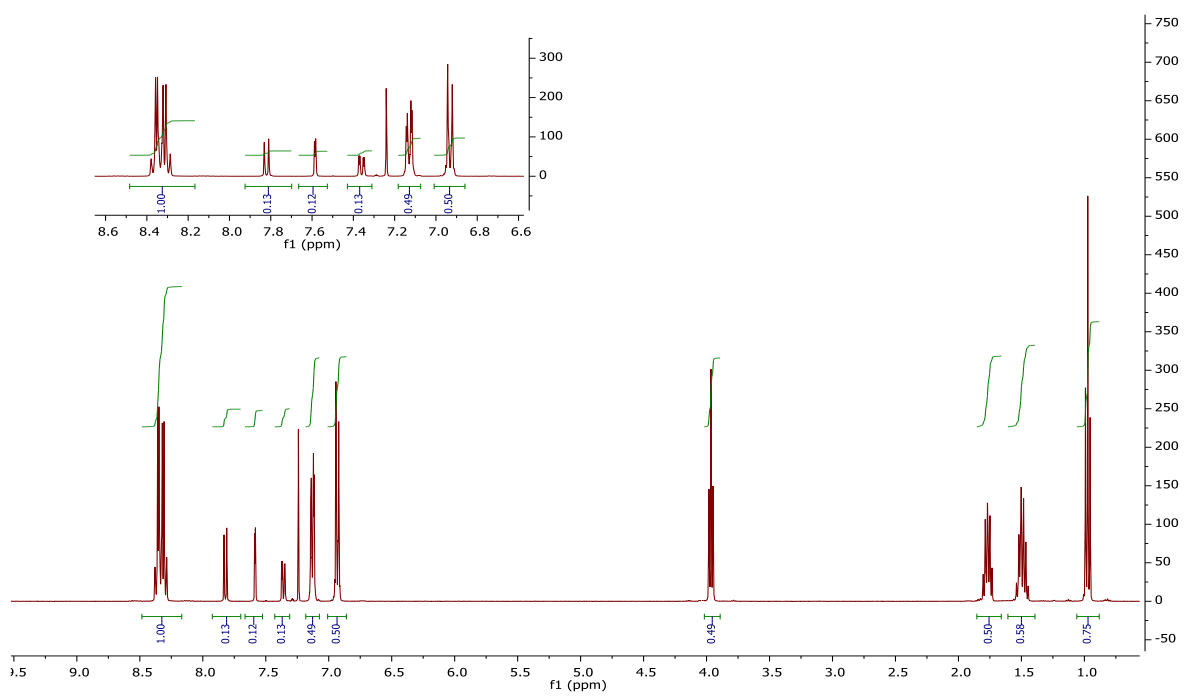


Figure S1b. ¹³C-NMR spectrum (100 MHz, CDCl_3) of **1/O2**.



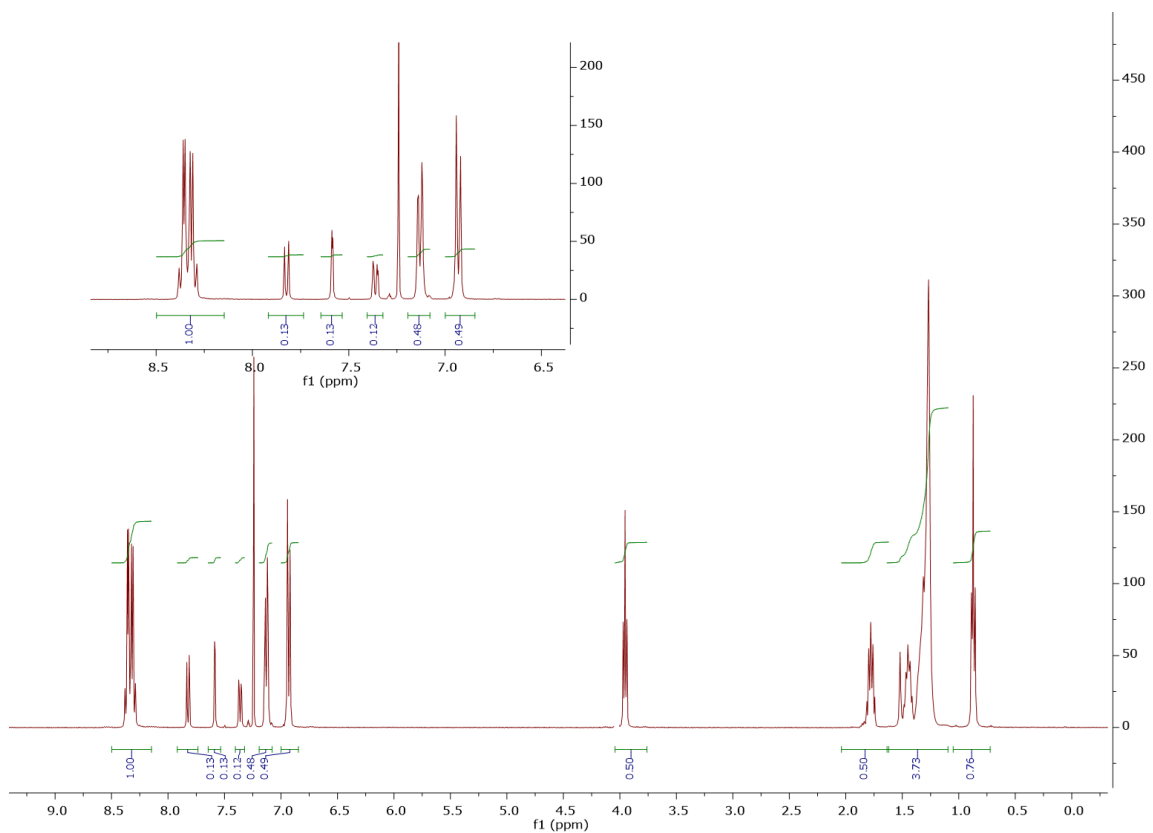


Figure S3a. ^1H -NMR spectrum (400 MHz, CDCl_3) of **1/O10**.

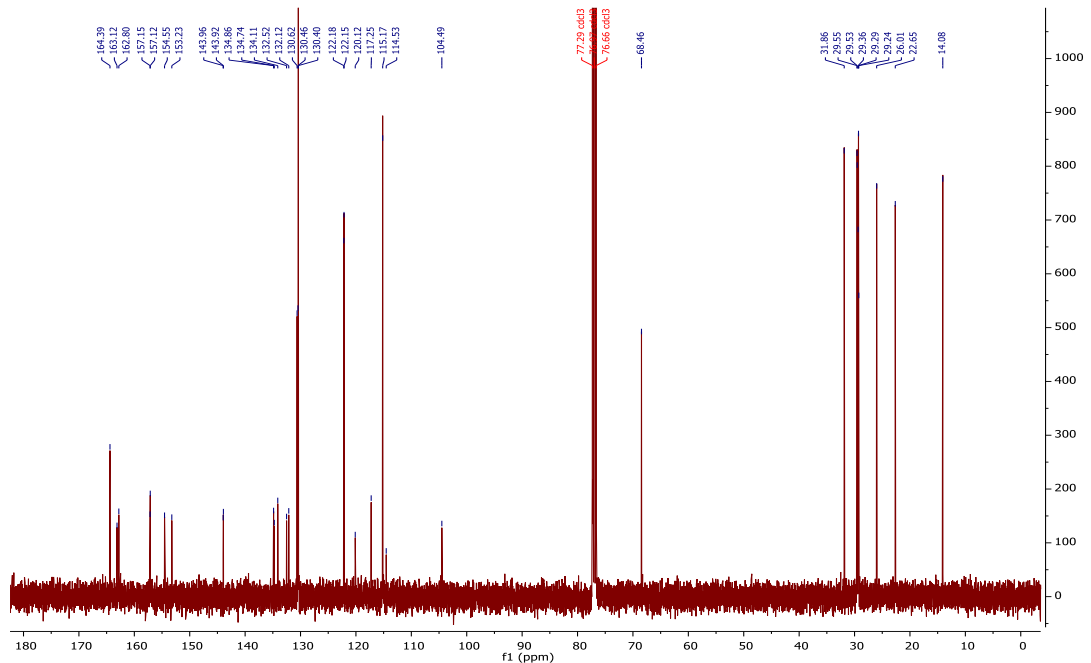


Figure S3b. ^{13}C -NMR spectrum (100 MHz, CDCl_3) of **1/O10**.

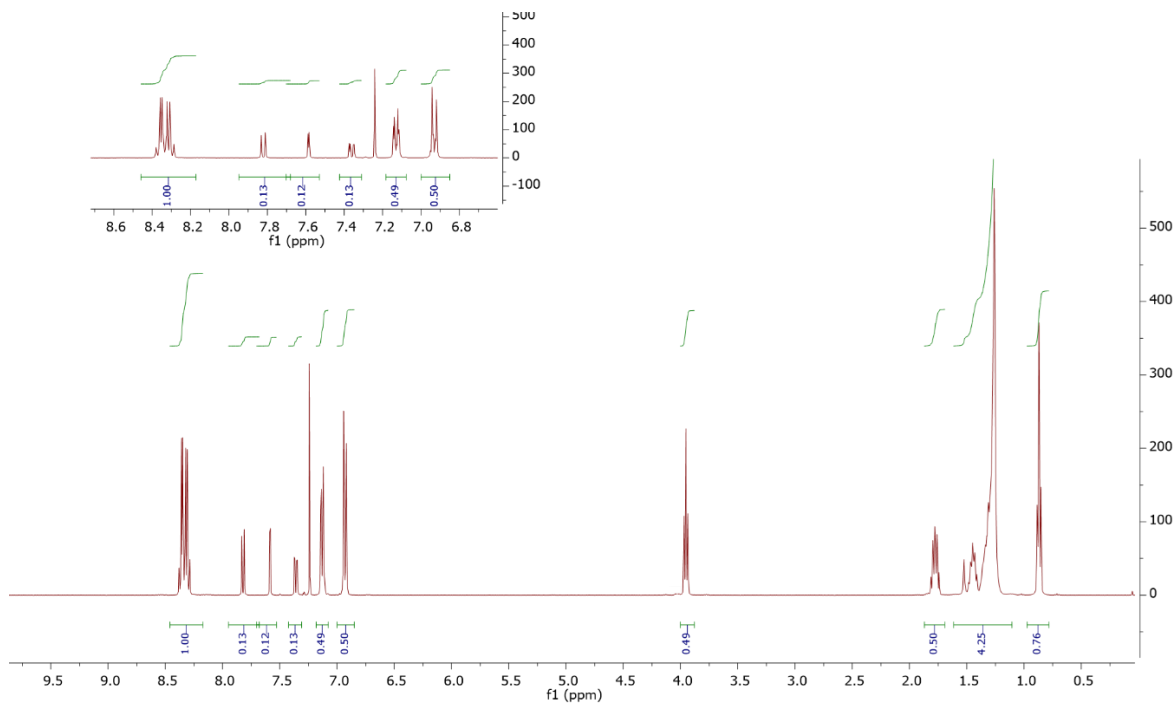


Figure S4a. ^1H -NMR spectrum (400 MHz, CDCl_3) of **1/O11**.

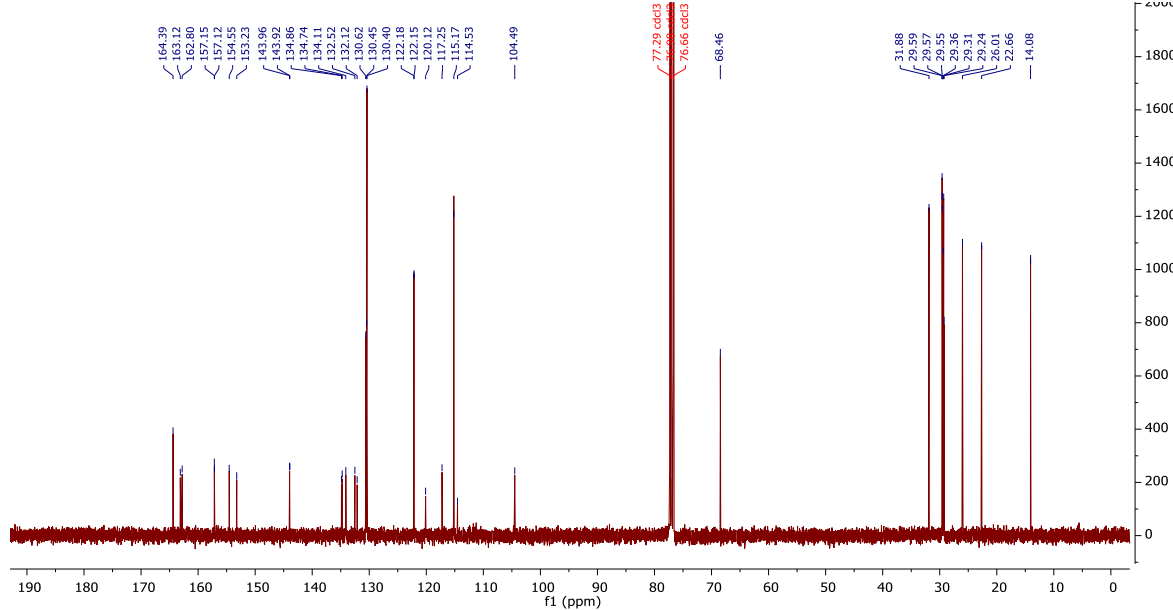


Figure S4b. ^{13}C -NMR spectrum (100 MHz, CDCl_3) of **1/O11**.

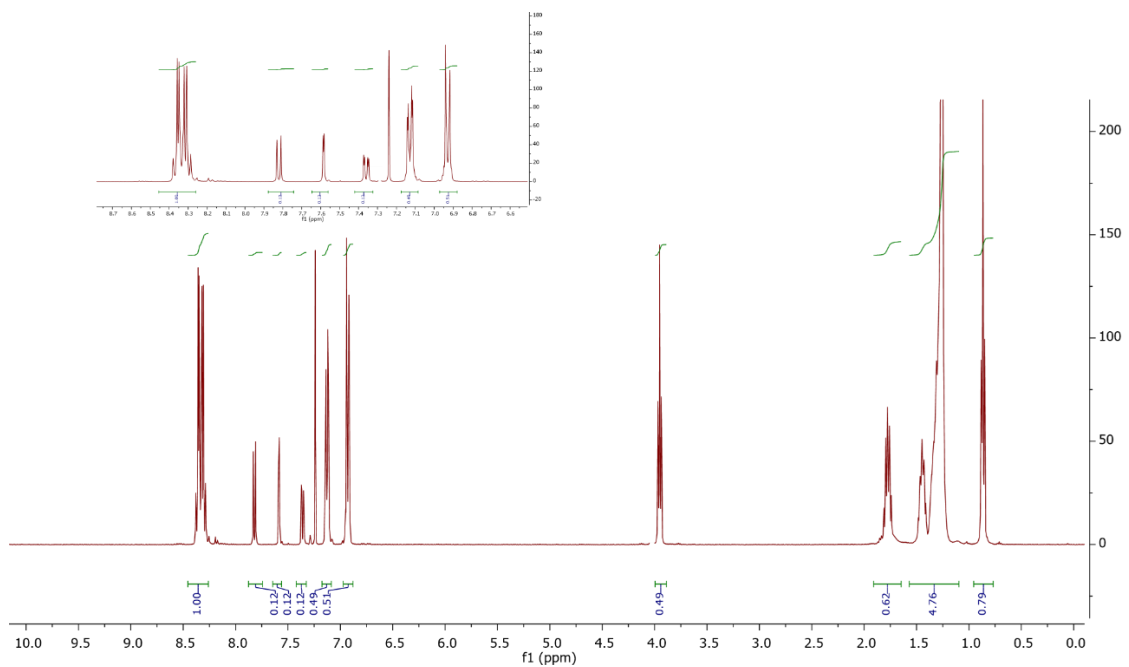


Figure S5a. ^1H -NMR spectrum (600 MHz, CDCl_3) of **1/O12**.

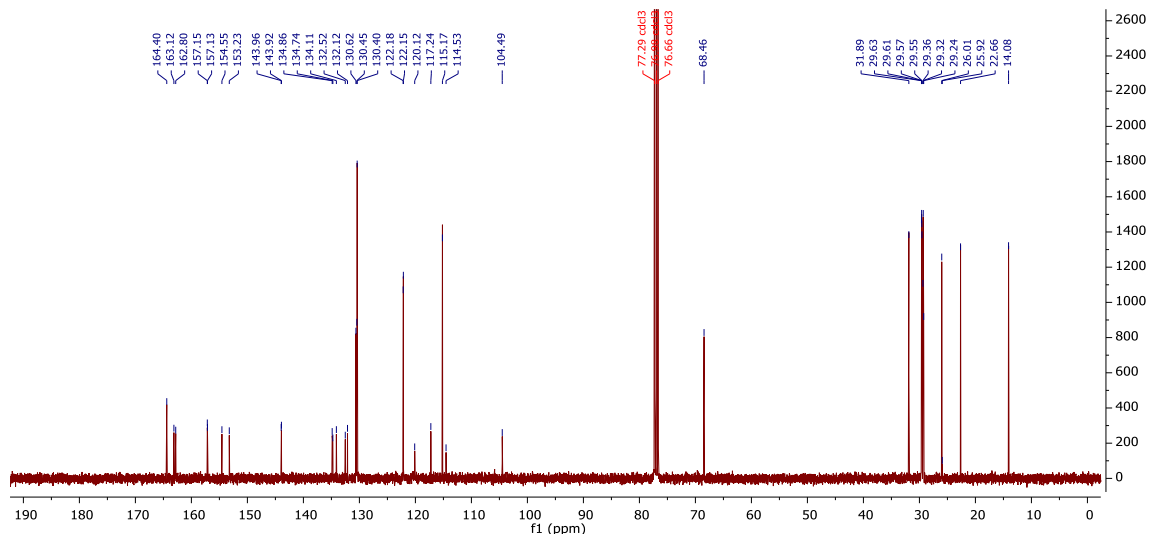


Figure S5b. ^{13}C -NMR spectrum (100 MHz, CDCl_3) of **1/O12**.

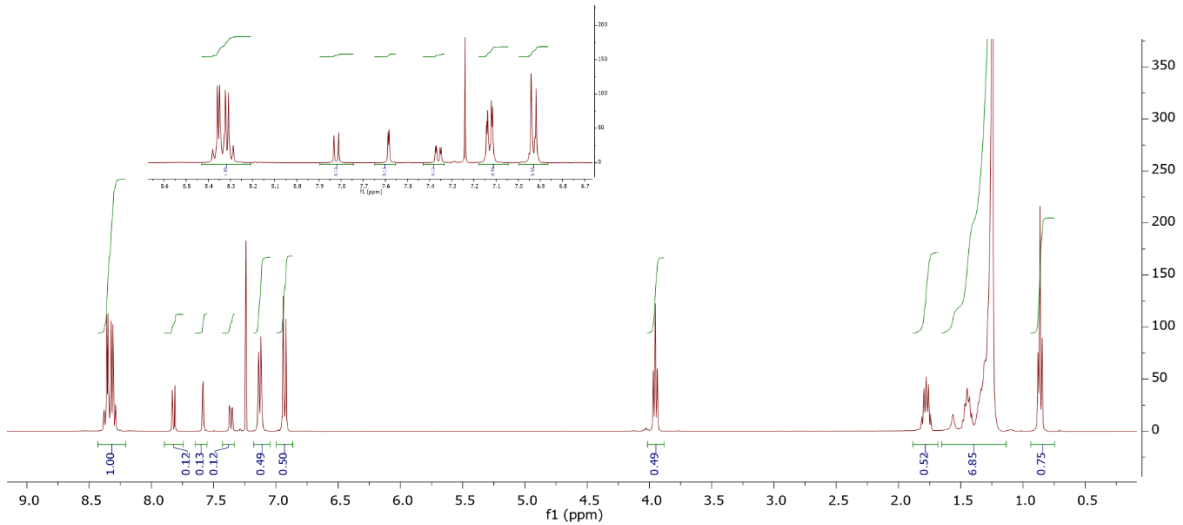


Figure S6a. ^1H -NMR spectrum (500 MHz, CDCl_3) of **1/O16**.

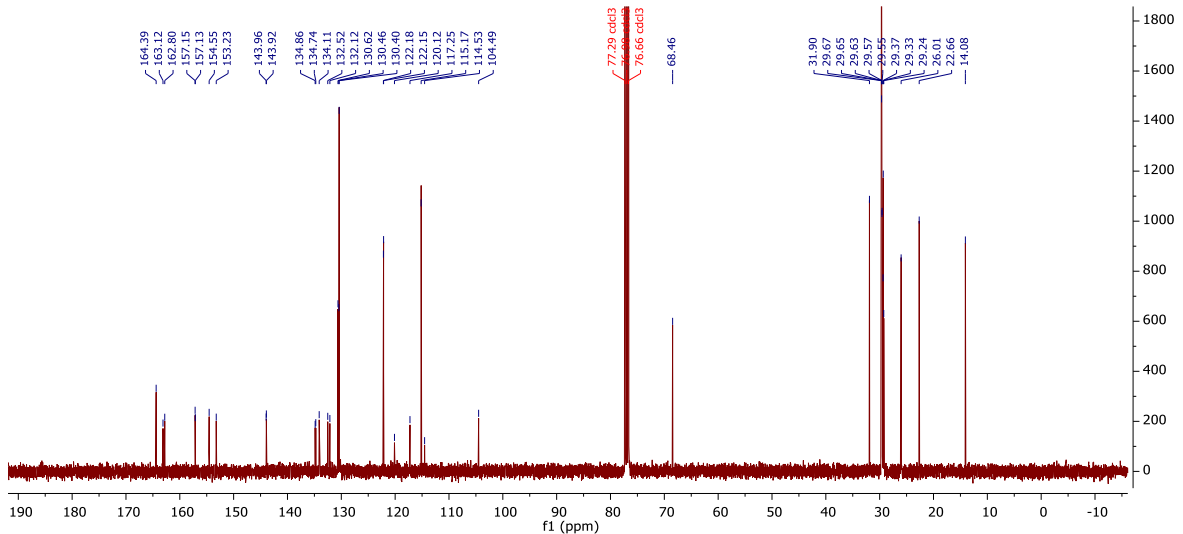


Figure S6b. ^{13}C -NMR spectrum (100 MHz, CDCl_3) of **1/O16**.

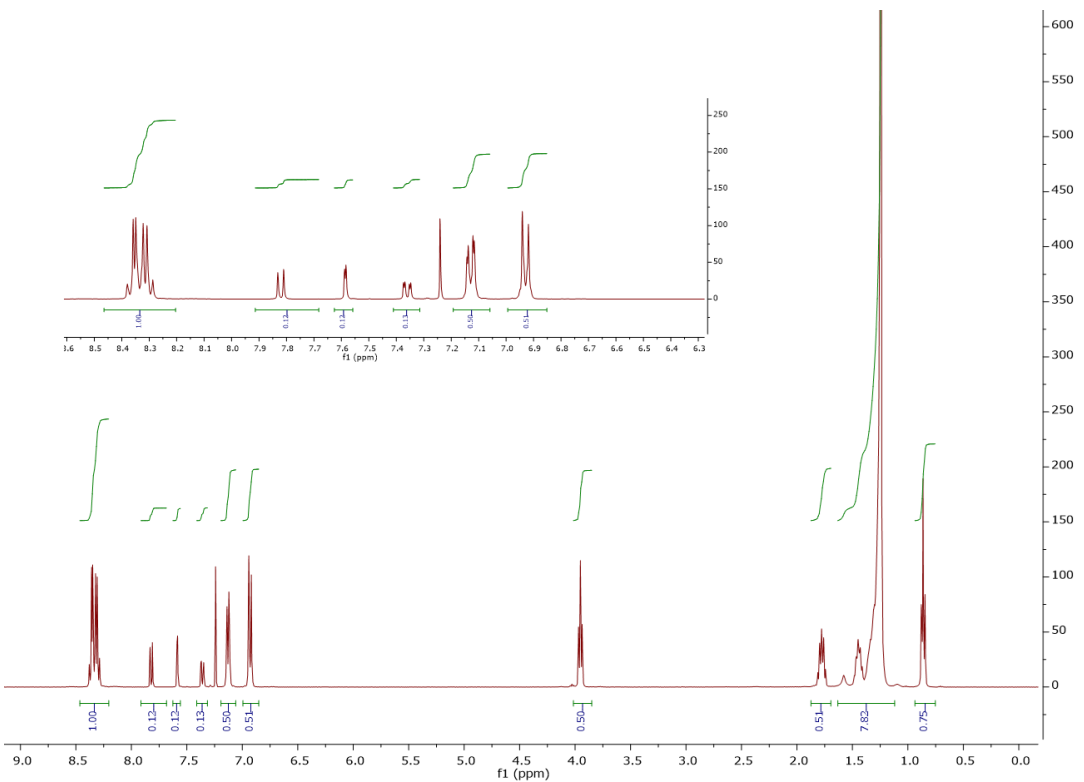
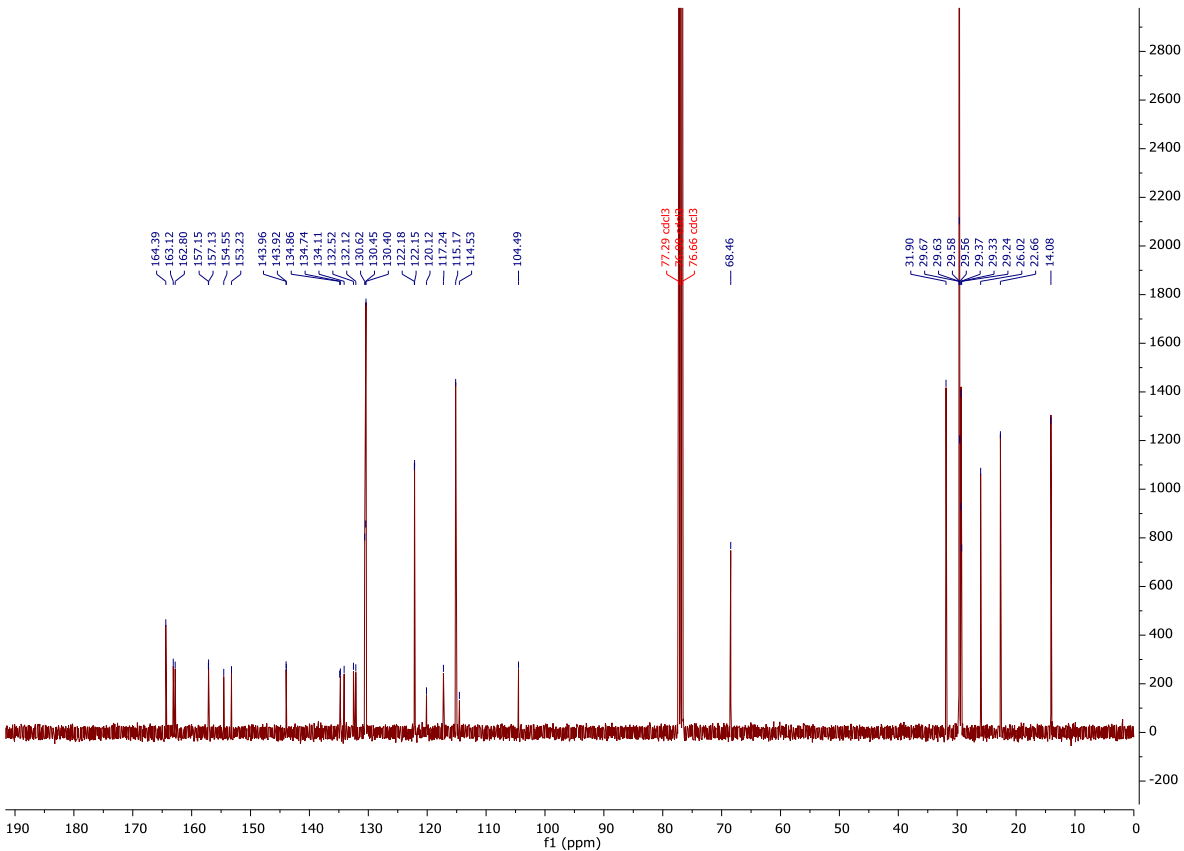


Figure S7. ^1H -NMR spectrum (400 MHz, CDCl_3) of **1/O18**.



2. Investigation methods

The self-assembly of compounds **1/On** was studied by polarizing optical microscopy (POM), differential scanning calorimetry (DSC), X-ray diffraction, electro-optical investigations and some of them by dielectric studies, second harmonic generation (SHG) and free-standing films. All compounds are thermally stable as confirmed by the reproducibility of thermograms in several heating and cooling cycles.

POM investigations were conducted using a Mettler FP-82 HT hot stage and a control unit in conjunction with a Nikon Optiphot-2 polarizing microscope. The associated enthalpies were obtained from the DSC-thermograms which were recorded on a Perkin-Elmer DSC-7 with 10 K min^{-1} heating and cooling rate.

X-ray diffraction patterns were recorded with a 2D detector (Vantec 500, Bruker for $n = 2\text{-}6, 18, 20$ and HI-star, Siemens for $n = 11\text{-}16$). Ni filtered and pin hole collimated CuK_α radiation was used. The exposure time was 30 min and the sample to detector distance was 8.95 cm (WAXS) and 26.7 cm (SAXS) respectively. Uniform orientation was achieved by magnetic alignment in a capillary (1T, $n = 2\text{,}4$) or by alignment on a flat substrate at the air-sample interface on top of a small droplet ($n = 6\text{-}20$). The samples were held on a temperature-controlled heating stage and the X-ray beam was parallel to the substrate.

The electro-optical switching characteristics were examined with the triangular-wave method using a home-made set-up in 6 μm polyimide coated indium tin oxide (ITO) cells, uniformly rubbed for planar alignment with a measuring area of 1 cm^2 , EHC Japan. The homeotropic alignment was achieved in 5 μm ITO cells with bare electrodes, EHC Japan.

Measurements of the optical second harmonic generation (SHG) were performed in non-treated (bare) ITO cells and cells with rubbed polyimide aligning layer. In both cell types we observed planar alignment. A Nd:YAG laser operating at $\lambda = 1064\text{ nm}$ (10 ns pulse width and 10 Hz repetition rate) was used. The primary beam was incident at an angle of 30° to the cell normal. The SHG signal was detected in transmission by a photomultiplier tube (Hamamatsu). The acquired signal was calibrated using a 50 μm reference quartz plate.

Dielectric measurements were performed on cooling runs in the frequency range of 100 Hz–10 MHz with the impedance analyzer Solartron 1260A or with High Resolution Impedance Analyser manufactured by Novocontrol technologies GmbH, Hundsagan, in a 12 μm gold cell.. Temperature control was achieved using Quatro Temperature Controller of the same Company with accuracy in temperature of $\pm 0.1\text{ }^\circ\text{C}$. Capacitance of the cell was carefully calibrated before being filled in the isotropic state and the measuring field was 0.5 Vrms. The dielectric data were fitted to Havriliak Negami equation using Novocontrol WINFIT programme. The dielectric relaxation frequency and the dielectric strength were calculated for one or more processes.

Freely suspended films were prepared by pulling the material in the smectic phase over a custom-made frame (2 mm x 5 mm) mounted in the heating stage. The film thickness was determined by the analysis of the reflected light spectra using a USB spectrometer.

3. Additional DSC traces

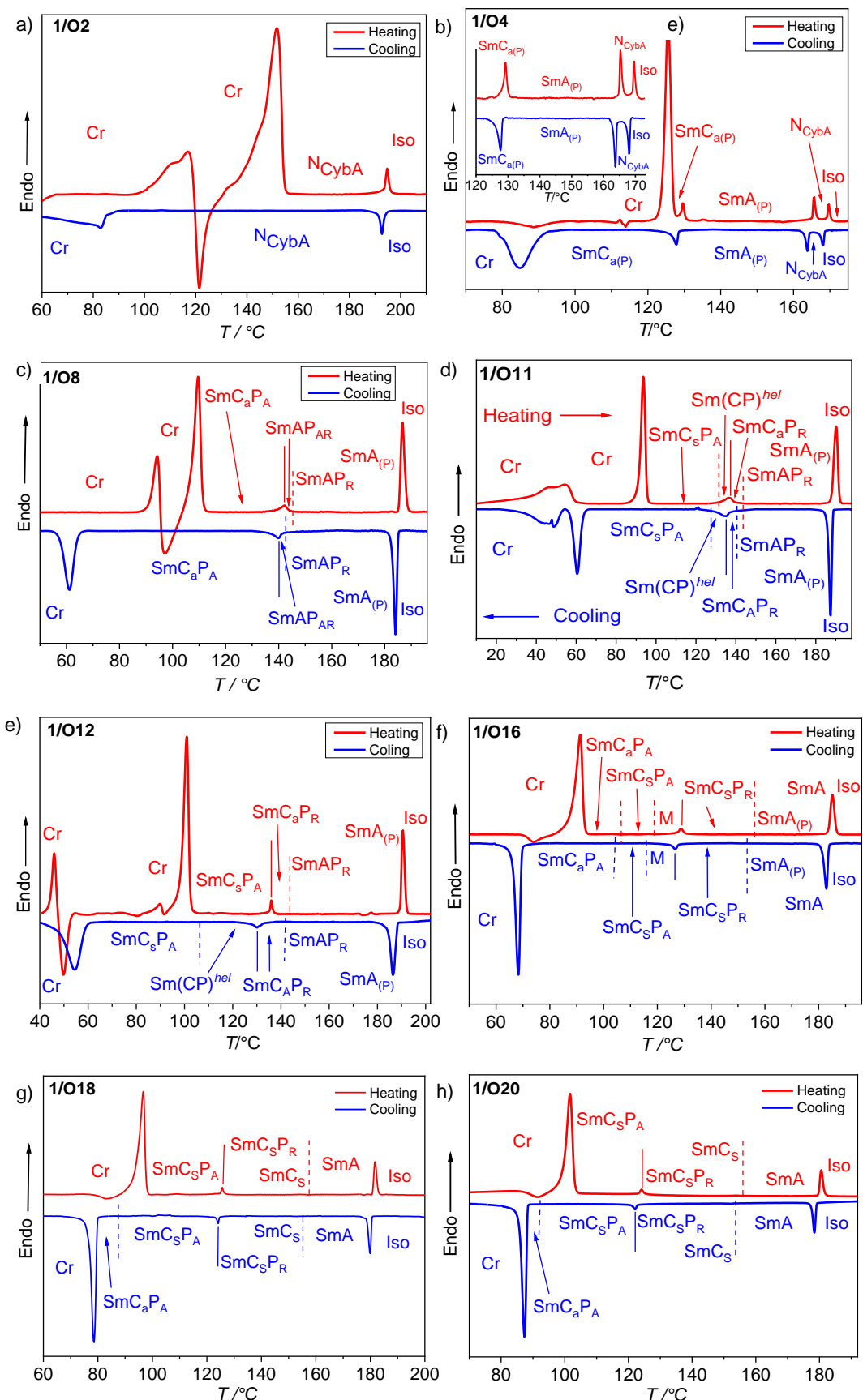


Figure S9. DSC heating and cooling traces at 10 K min^{-1} .

4. Additional XRD data

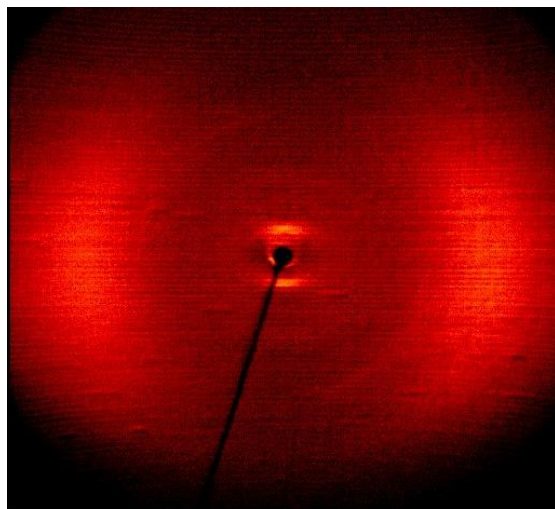


Figure S10. X-ray Diffraction pattern of the N phase of **1/O2** at 158 °C.

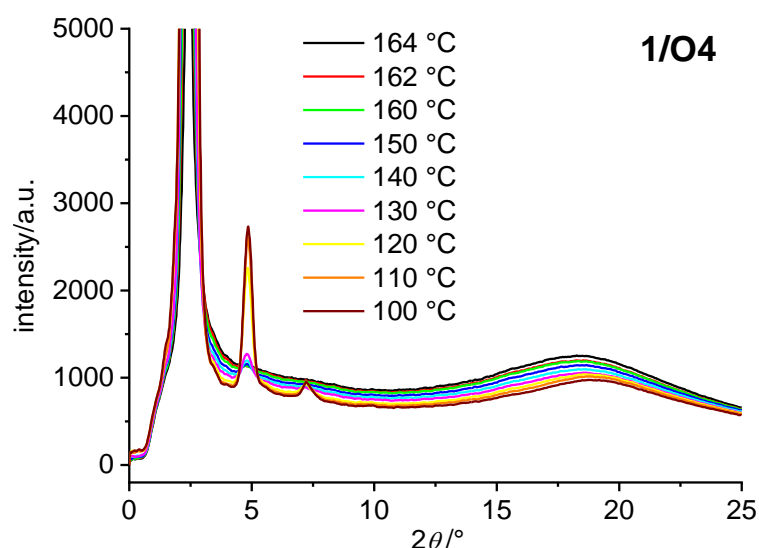


Figure S11. XRD patterns of **1/O4** depending on temperature.

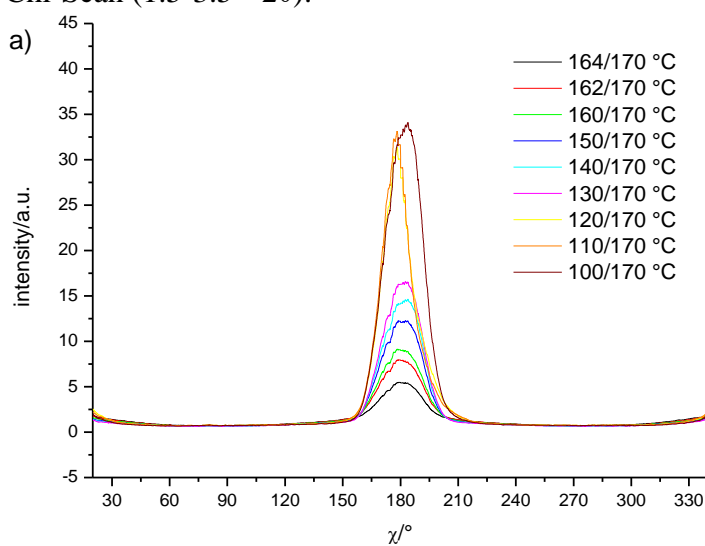
Table S1. SAXS data of **1/O4**.

T/°C	2 Theta/°	Theta/°	d /nm
164	2.465	1.233	3.58 (diff)
162	2.416	1.208	3.66
160	2.404	1.202	3.68
150	2.397	1.199	3.69
140	2.397	1.199	3.69
130	2.399	1.200	3.68
	4.789	2.395	1.85
120	2.414	1.207	3.66
	4.823	2.412	1.83
	7.209	3.605	1.23
110	2.425	1.213	3.64
	4.844	2.422	1.82
	7.254	3.627	1.22
100	2.434	1.217	3.63
	4.857	2.429	1.82
	7.278	3.639	1.22

Table S2. WAXS data of **1/O4**

T/°C	2 Theta/°	Theta/°	d /nm
164	18.420	9.210	0.482
162	18.450	9.225	0.481
160	18.480	9.240	0.480
150	18.540	9.270	0.479
140	18.600	9.300	0.477
130	18.670	9.335	0.475
120	18.780	9.390	0.472
110	18.890	9.445	0.470
100	18.950	9.475	0.468

Chi-Scan ($1.5\text{--}3.5^\circ 2\theta$):



Chi-Scan ($15\text{--}25^\circ 2\theta$)

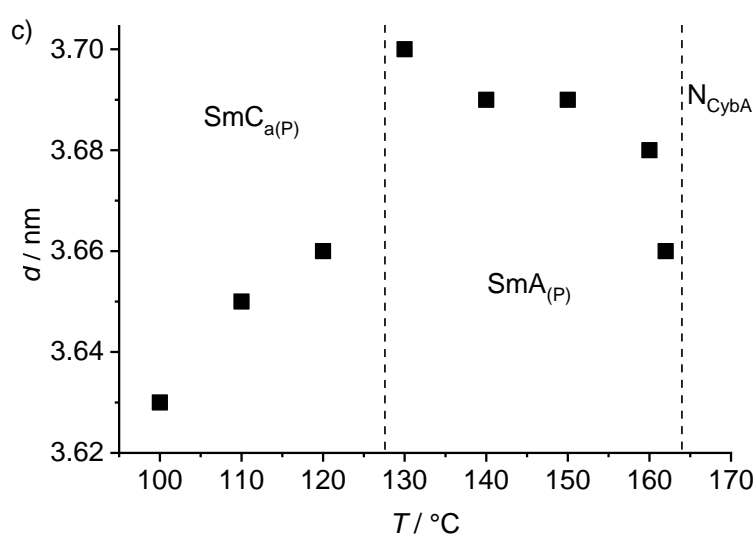
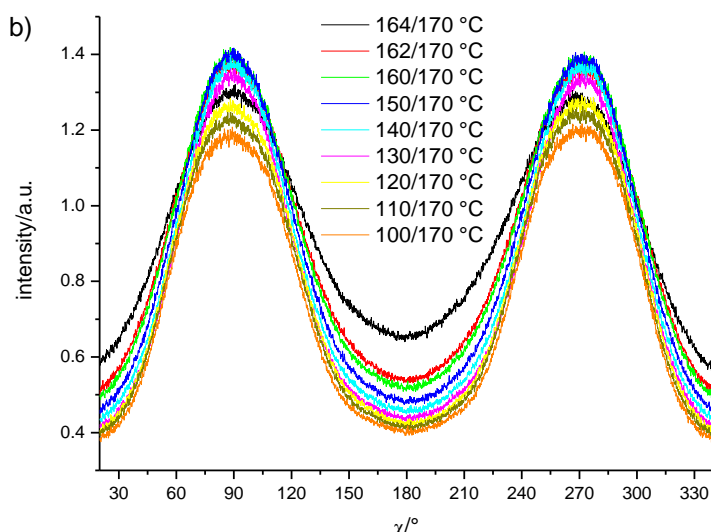


Figure S12. a) SAXS and b) WAXS chi scans, and c) temperature dependence of the d -values of **1/O4** as recorded on cooling; (P) indicates paraelectric phases.

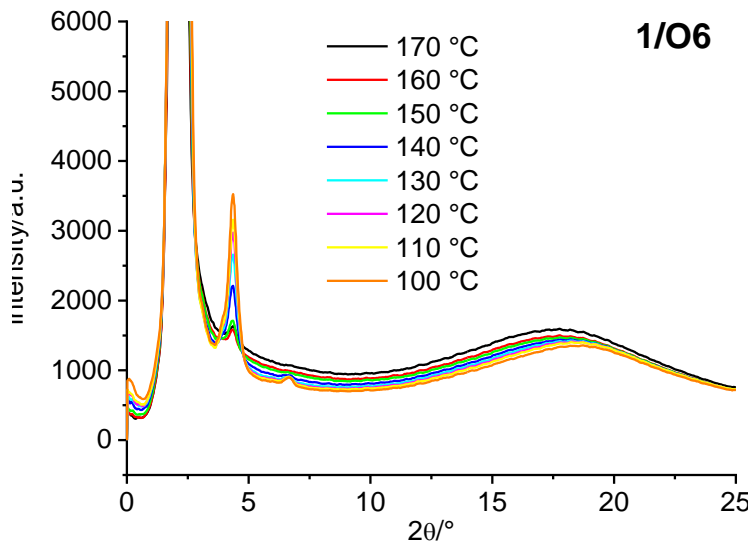


Figure S13. XRD patterns of **1/O6** depending on temperature.

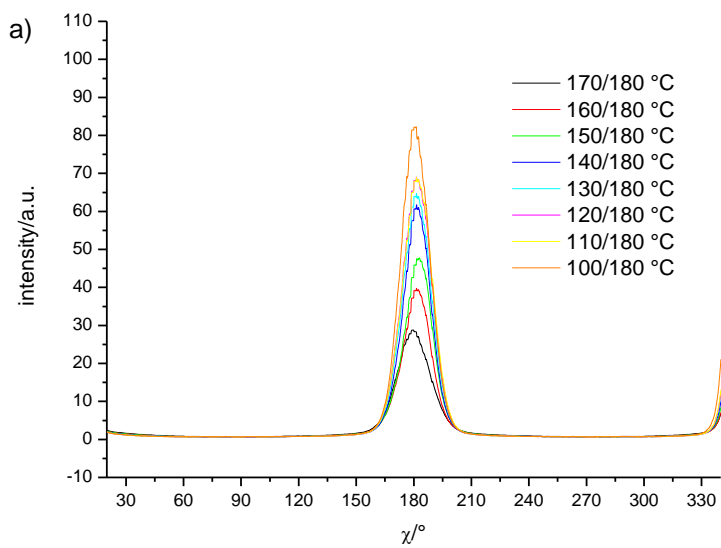
Table S3. Layer reflections of **1/O6** depending on temperatue.

T/°C	2 Theta/°	Theta/°	d /nm
160	2.210	1.105	3.997
155	2.209	1.105	3.999
150	2.207	1.104	4.003
148	2.208	1.104	4.001
146	2.211	1.106	3.996
144	2.214	1.107	3.990
142	2.218	1.109	3.983
140	2.220	1.110	3.979
138	2.223	1.112	3.974
136	2.224	1.112	3.972
134	2.226	1.113	3.969
132	2.228	1.114	3.965
130	2.228	1.114	3.965
128	2.229	1.115	3.963
126	2.231	1.116	3.960
124	2.231	1.116	3.960
120	2.233	1.117	3.956
115	2.235	1.118	3.953
110	2.237	1.119	3.949
105	2.238	1.119	3.947
100	2.240	1.120	3.944
95	2.209	1.105	3.999
90	2.207	1.104	4.003

Table S4. WAXS data of **1/O6**

T/°C	2 Theta/°	Theta/°	d /nm
170	17.660	8.830	0.502
160	17.730	8.865	0.500
150	17.830	8.915	0.497
140	17.940	8.970	0.494
130	18.050	9.025	0.491
120	18.150	9.075	0.489
110	18.240	9.120	0.486
100	18.360	9.180	0.483

Chi-Scan ($1-3^\circ 2\theta$):



Chi-Scan ($14-24^\circ 2\theta$):

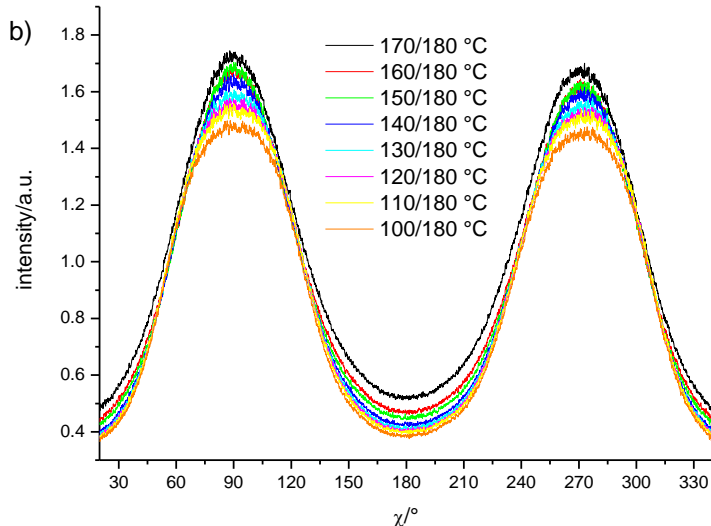


Figure S14. a) SAXS and b) WAXS chi scans of **1/O6** as recorded on cooling.

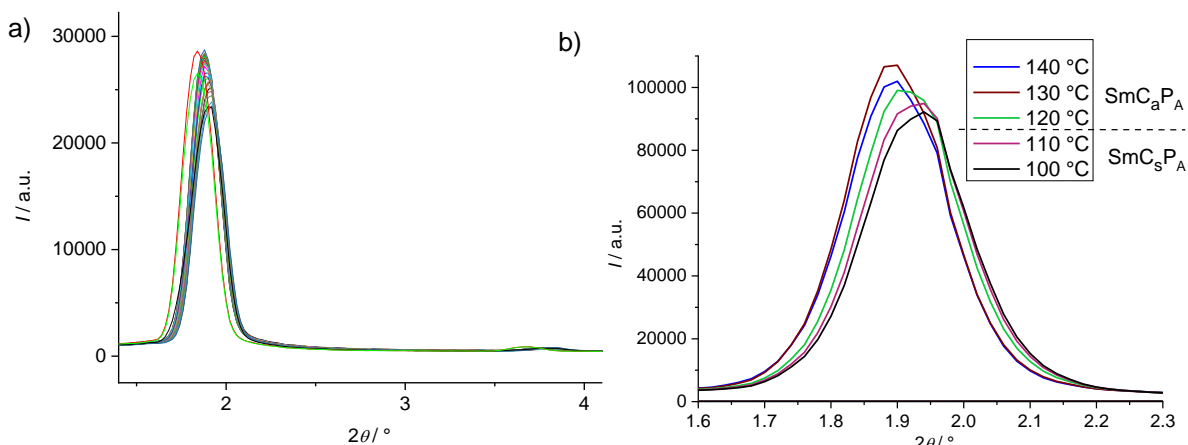


Figure S15. a) SAXS patterns of **1/O10** depending on temperature and b) temperature dependence of the layer reflection around the anticlinic synclinic transition.

Table S5. Layer reflections of **1/O10** depending on temperature.

T/°C	2 Theta/°	Theta/°	d /nm
160	1.907	0.954	4.633
155	1.901	0.951	4.647
150	1.895	0.948	4.662
148	1.892	0.946	4.669
146	1.890	0.945	4.674
144	1.887	0.944	4.682
142	1.886	0.943	4.684
140	1.884	0.942	4.689
138	1.882	0.941	4.694
136	1.881	0.941	4.697
134	1.881	0.941	4.697
132	1.881	0.941	4.697
130	1.881	0.941	4.697
128	1.882	0.941	4.694
126	1.883	0.942	4.692
124	1.885	0.943	4.687
120	1.889	0.945	4.677
115	1.896	0.948	4.659
110	1.901	0.951	4.647
105	1.904	0.952	4.640
100	1.907	0.954	4.633
95	1.910	0.955	4.625
90	1.912	0.956	4.620
85	1.896	0.948	4.659
80	1.843	0.922	4.793
70	1.843	0.922	4.793

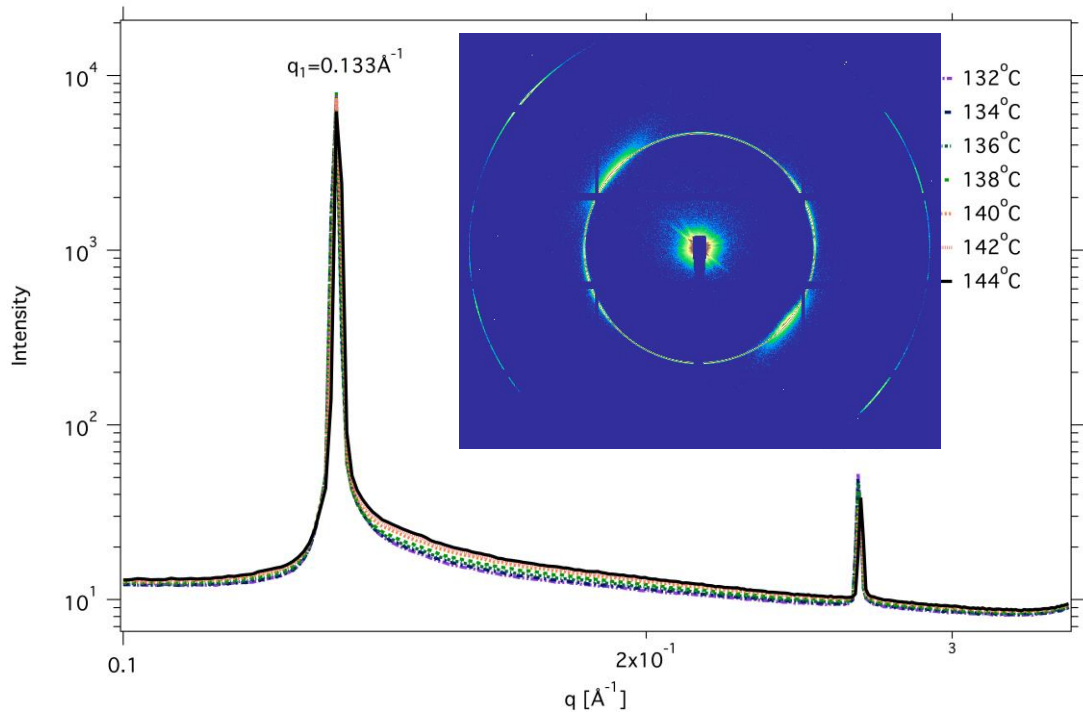


Figure S16. Synchrotron-SAXS patterns of **1/O10** in the temperature range of the M phase.

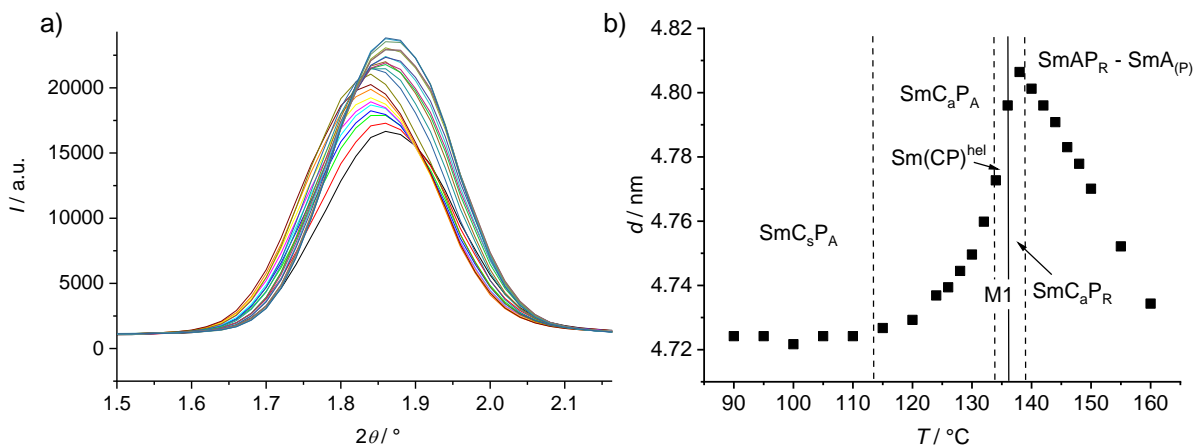


Figure S17. a) SAXS peak and b) d-values of **1/O11** depending on temperature (recorded on cooling); the solid line indicates the Curie temperature.

Table S6. Layer reflections of **1/O11** depending on temperature.

$T / {}^\circ\text{C}$	2 Theta/°	Theta/°	d / nm
160	1.866	0.933	4.734
155	1.859	0.930	4.752
150	1.852	0.926	4.770
148	1.849	0.925	4.778
146	1.847	0.924	4.783
144	1.844	0.922	4.791
142	1.842	0.921	4.796
140	1.840	0.920	4.801
138	1.838	0.919	4.806
136	1.842	0.921	4.796
134	1.851	0.926	4.773
132	1.856	0.928	4.760
130	1.860	0.930	4.750
128	1.862	0.931	4.744
126	1.864	0.932	4.739
124	1.865	0.933	4.737
120	1.868	0.934	4.729
115	1.869	0.935	4.727
110	1.870	0.935	4.724
105	1.870	0.935	4.724
100	1.871	0.936	4.722
95	1.870	0.935	4.724
90	1.870	0.935	4.724

Table S7. Layer reflections of **1/O12** measured on cooling (left) and heating (right).

T/°C	2 Theta/°	Theta/°	d /nm
160	1.814	0.907	4.870
155	1.806	0.903	4.892
150	1.799	0.900	4.911
148	1.796	0.898	4.919
146	1.793	0.897	4.927
144	1.790	0.895	4.935
142	1.787	0.894	4.944
140	1.784	0.892	4.952
138	1.782	0.891	4.957
136	1.779	0.890	4.966
134	1.780	0.890	4.963
132	1.788	0.894	4.941
130	1.795	0.898	4.922
128	1.797	0.899	4.916
126	1.799	0.900	4.911
124	1.800	0.900	4.908
120	1.801	0.901	4.905
115	1.801	0.901	4.905
110	1.800	0.900	4.908
105	1.798	0.899	4.913
100	1.796	0.898	4.919
95	1.794	0.897	4.924
90	1.791	0.896	4.933

T/°C	2 Theta/°	Theta/°	d /nm
160	1.813	0.907	4.873
155	1.804	0.902	4.897
150	1.797	0.899	4.916
148	1.794	0.897	4.924
146	1.791	0.896	4.933
144	1.788	0.894	4.941
142	1.785	0.893	4.949
140	1.782	0.891	4.957
138	1.780	0.890	4.963
136	1.777	0.889	4.971
134	1.777	0.889	4.971
132	1.784	0.892	4.952
130	1.791	0.896	4.933
128	1.795	0.898	4.922
126	1.797	0.899	4.916
124	1.798	0.899	4.913
120	1.799	0.900	4.911
115	1.800	0.900	4.908
110	1.799	0.900	4.911
105	1.797	0.899	4.916
100	1.796	0.898	4.919
95	1.793	0.897	4.927

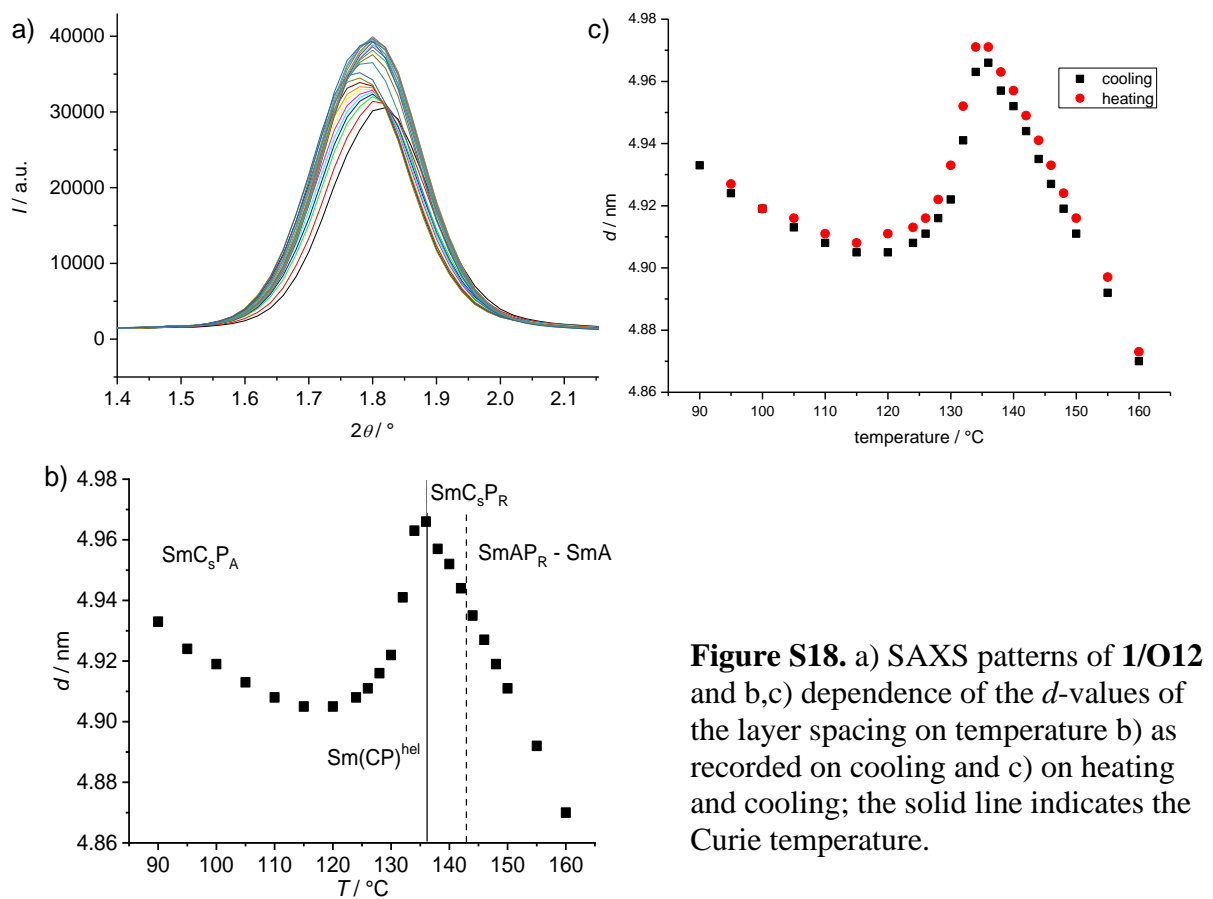


Figure S18. a) SAXS patterns of **1/O12** and b,c) dependence of the d -values of the layer spacing on temperature b) as recorded on cooling and c) on heating and cooling; the solid line indicates the Curie temperature.

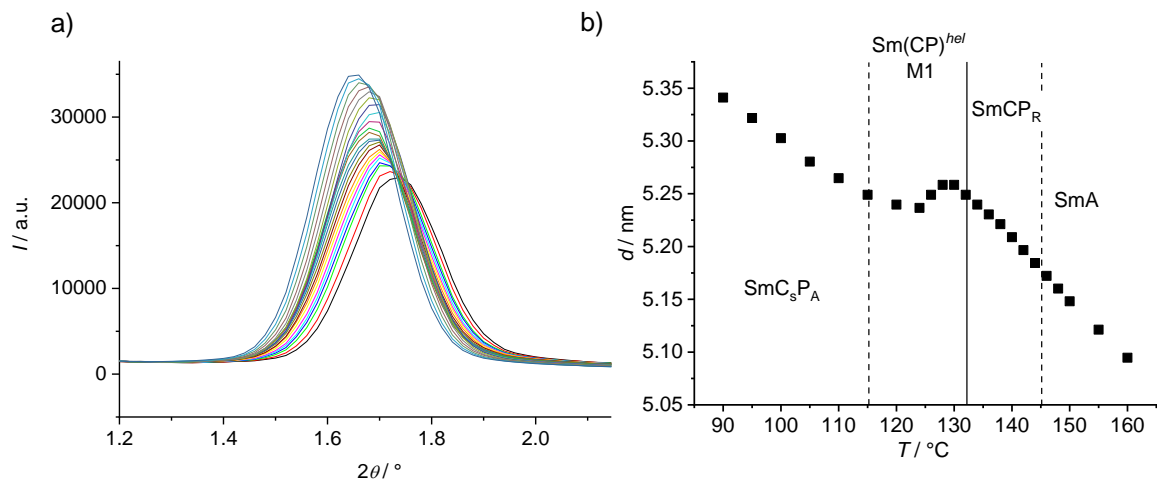


Figure S19. a) SAXS patterns and b) d -values of the layer spacing of **1/O14** depending on temperature; the solid line indicates the Curie temperature.

Table S8. Layer reflections of **1/O14** measured on cooling.

$T/^\circ\text{C}$	2 Theta/°	Theta/°	d/nm
160	1.734	0.867	5.095
155	1.725	0.863	5.121
150	1.716	0.858	5.148
148	1.712	0.856	5.160
146	1.708	0.854	5.172
144	1.704	0.852	5.184
142	1.700	0.850	5.197
140	1.696	0.848	5.209
138	1.692	0.846	5.221
136	1.689	0.845	5.230
134	1.686	0.843	5.240
132	1.683	0.842	5.249
130	1.680	0.840	5.258
128	1.680	0.840	5.258
126	1.683	0.842	5.249
124	1.687	0.844	5.237
120	1.686	0.843	5.240
115	1.683	0.842	5.249
110	1.678	0.839	5.265
105	1.673	0.837	5.280
100	1.666	0.833	5.303
95	1.660	0.830	5.322
90	1.654	0.827	5.341

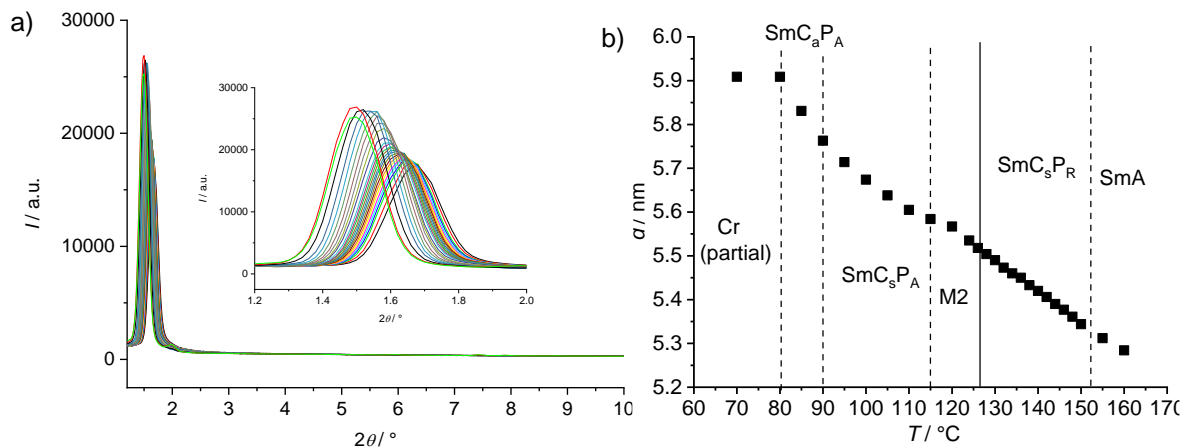


Figure S20. a) SAXS patterns and b) d -values of the layer spacing of **1/O16** depending on temperature (measured on cooling); the solid line indicates the Curie temperature.

Table S9. Layer reflections of **1/O16** measured on cooling.

$T/{}^\circ\text{C}$	2 Theta/°	Theta/°	d/nm
160	1.672	0.836	5.284
155	1.663	0.832	5.312
150	1.653	0.827	5.344
148	1.648	0.824	5.361
146	1.643	0.822	5.377
144	1.639	0.820	5.390
142	1.634	0.817	5.406
140	1.630	0.815	5.420
138	1.626	0.813	5.433
136	1.621	0.811	5.450
134	1.618	0.809	5.460
132	1.614	0.807	5.473
130	1.609	0.805	5.490
128	1.605	0.803	5.504
126	1.601	0.801	5.518
124	1.596	0.798	5.535
120	1.587	0.794	5.567
115	1.582	0.791	5.584
110	1.576	0.788	5.605
105	1.567	0.784	5.638
100	1.557	0.779	5.674
95	1.546	0.773	5.714
90	1.533	0.767	5.763
85	1.515	0.758	5.831
80	1.495	0.748	5.909
70	1.495	0.748	5.909

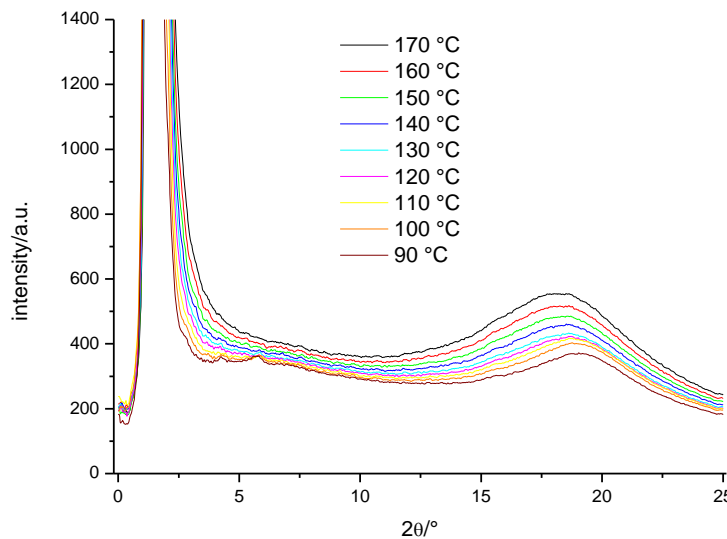


Figure S21. XRD patterns of **1/O18** depending on temperature, the small peaks at 90 and 100 °C are attributed to partial crystallization (measured on cooling).

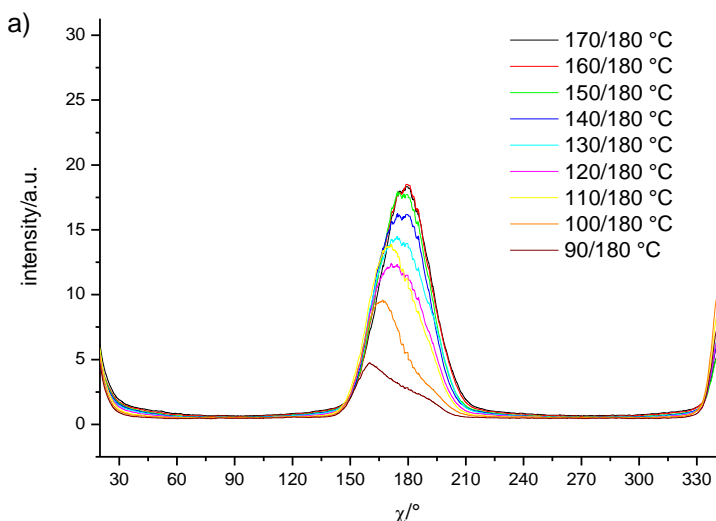
Table S10. SAXS data of **1/O18**.

T/°C	2 Theta/°	Theta/°	d /nm
170	1.599	0.800	5.525
160	1.570	0.785	5.627
150	1.549	0.775	5.703
140	1.532	0.766	5.766
130	1.511	0.756	5.847
120	1.491	0.746	5.925
110	1.474	0.737	5.993
100	1.451	0.726	6.088
90	1.446	0.723	6.109

Table S11. WAXS data of **1/O18**.

T/°C	2 Theta/°	Theta/°	d /nm
170	18.220	9.110	0.487
160	18.310	9.155	0.485
150	18.400	9.200	0.482
140	18.480	9.240	0.480
130	18.600	9.300	0.477
120	18.710	9.355	0.474
110	18.860	9.430	0.471
100	18.970	9.485	0.470
90	19.120	9.560	0.466

Chi-Scan ($1\text{-}3$ $^{\circ}$ 2θ):



Chi-Scan ($14\text{-}24$ $^{\circ}$ 2θ):

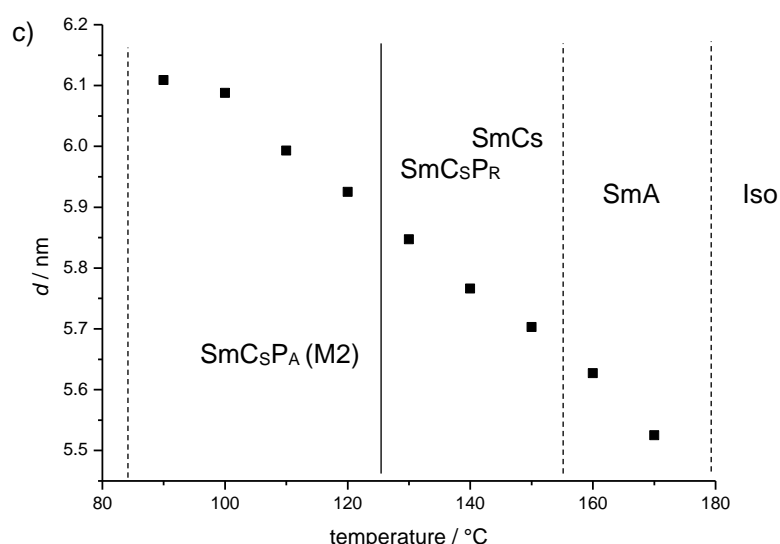
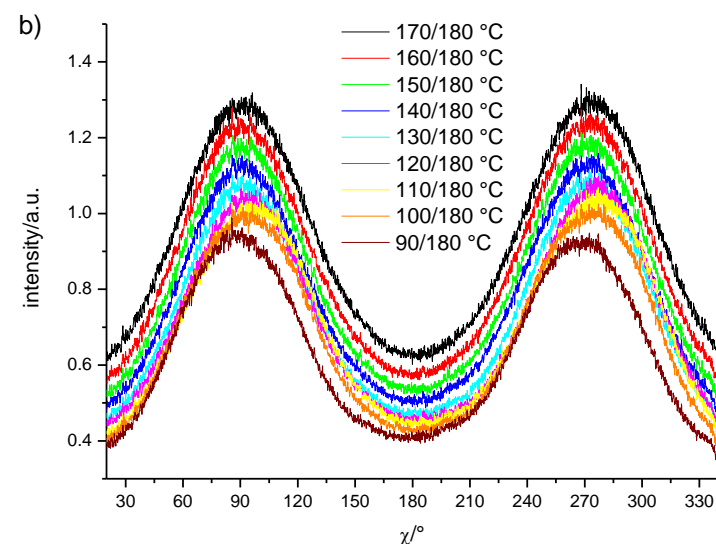


Figure S22. a) SAXS and b) WAXS chi scans, and c) temperature dependence of the d -values of **1/O18** as recorded on cooling; the M2 phase can coexist with, or replace SmCsP_A close to the Curie temperature; the solid line indicates the Curie temperature.

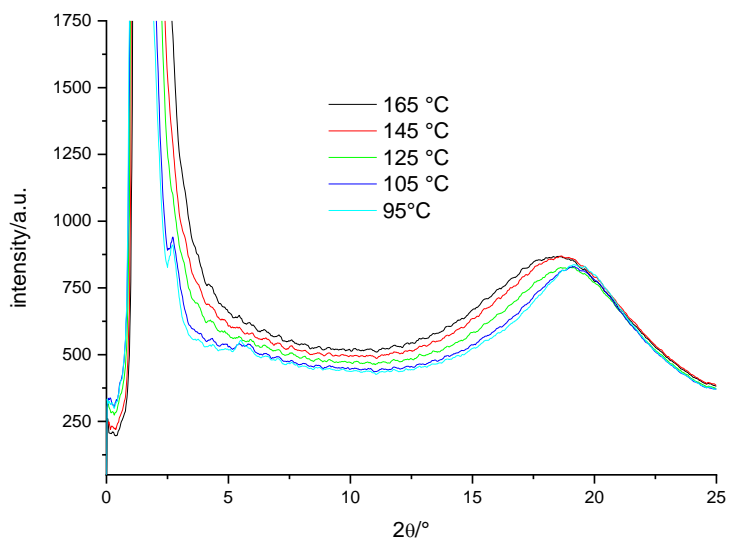


Figure S23. XRD patterns of **1/O20** recorded on cooling, the emerging peaks at 95 and 105 °C are attributed to partial crystallization.

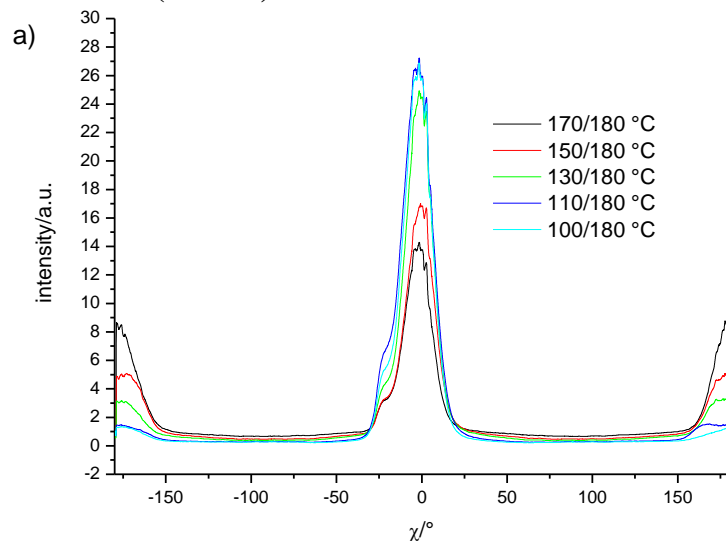
Table S12. SAXS data of **1/O20**.

T/°C	2 Theta/°	Theta/°	d /nm
170	1.621	0.811	5.450
150	1.551	0.776	5.696
130	1.516	0.758	5.827
110	1.448	0.724	6.101
100	1.411	0.706	6.261

Table S13. WAXS data of **1/O20**

T/°C	2 Theta/°	Theta/°	d /nm
170	18.400	9.200	0.482
150	18.610	9.305	0.477
130	18.810	9.405	0.472
110	19.060	9.530	0.466
100	19.180	9.590	0.463

Chi-Scan ($1\text{-}3^\circ$ 2θ):



Chi-Scan ($14\text{-}24^\circ$ 2θ):

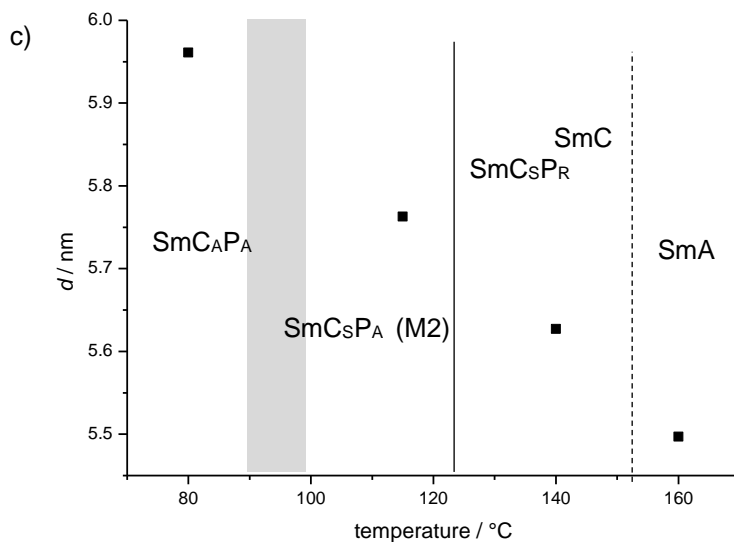
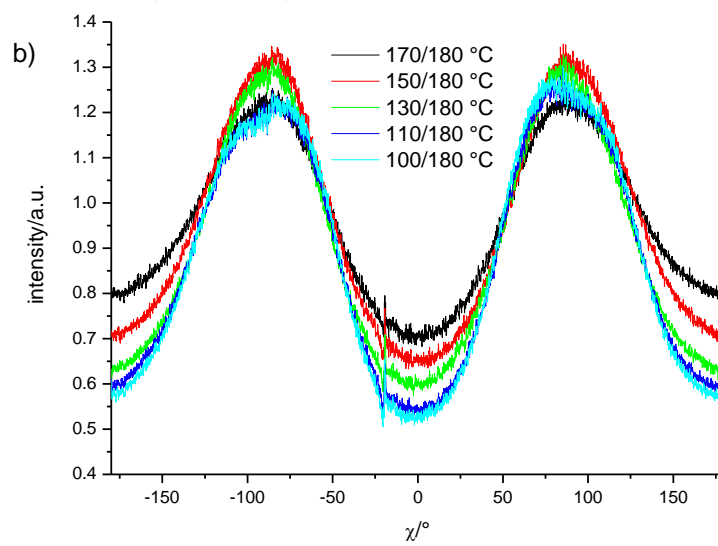


Figure S24. a) SAXS and b) WAXS chi scans, and c) temperature dependence of the d -values of **1/O20** as recorded on cooling; the M2 phase can coexist with, or replace SmCsPA close to the Curie temperature; the solid line indicates the Curie temperature.

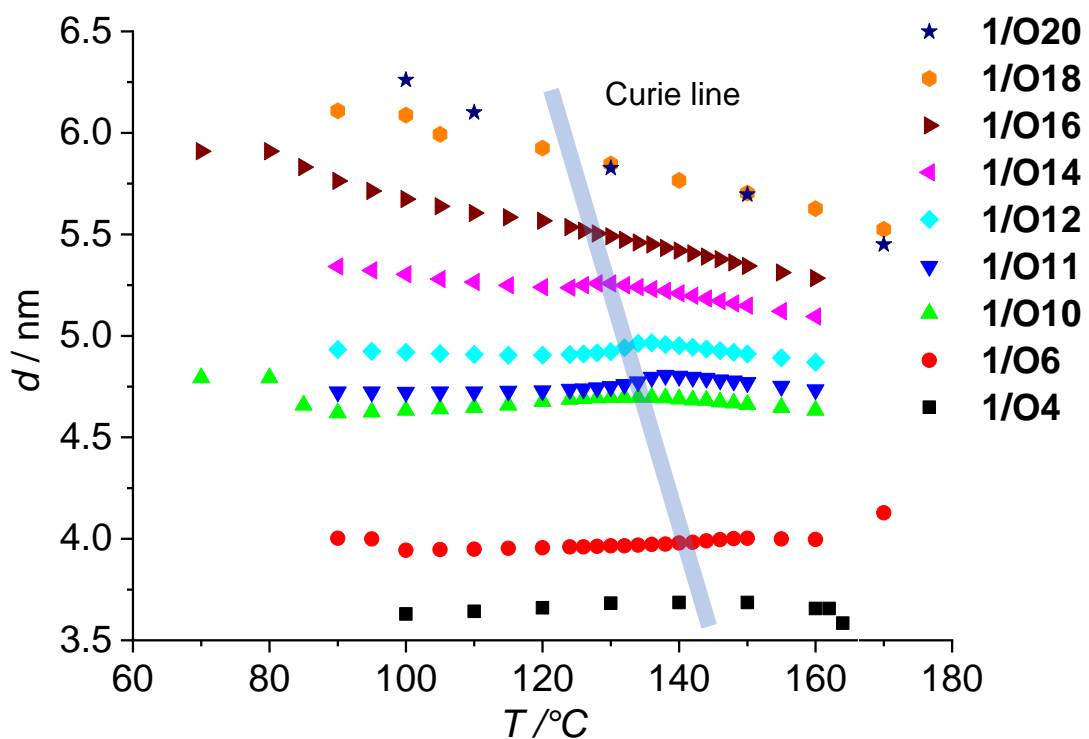


Figure S25. Comparison of the $d = f(T)$ curves of the layer spacing shows a change of the slope below the Curie temperature from negative to positive with increasing n and $n = 14$ representing the borderline case. Moreover, the temperature dependence of the layer spacing becomes larger with growing chain length. This might be interpreted as a result of the alkyl chain stretching at lower temperature. Because longer chains can assume more different conformations, for these compounds the reduction of conformational freedom has a stronger effect on d . Though in principle there could be an additional contribution of a decreasing tilt of the aromatic cores at lower temperature, there is no indication for this in the optical investigations of circular domains. It even appears the other way around, there is an increase of the tilt at the SmC-SmCP_R transition, but no recognizable change of the tilt on further cooling.

5. Additional optical and electrooptic investigations

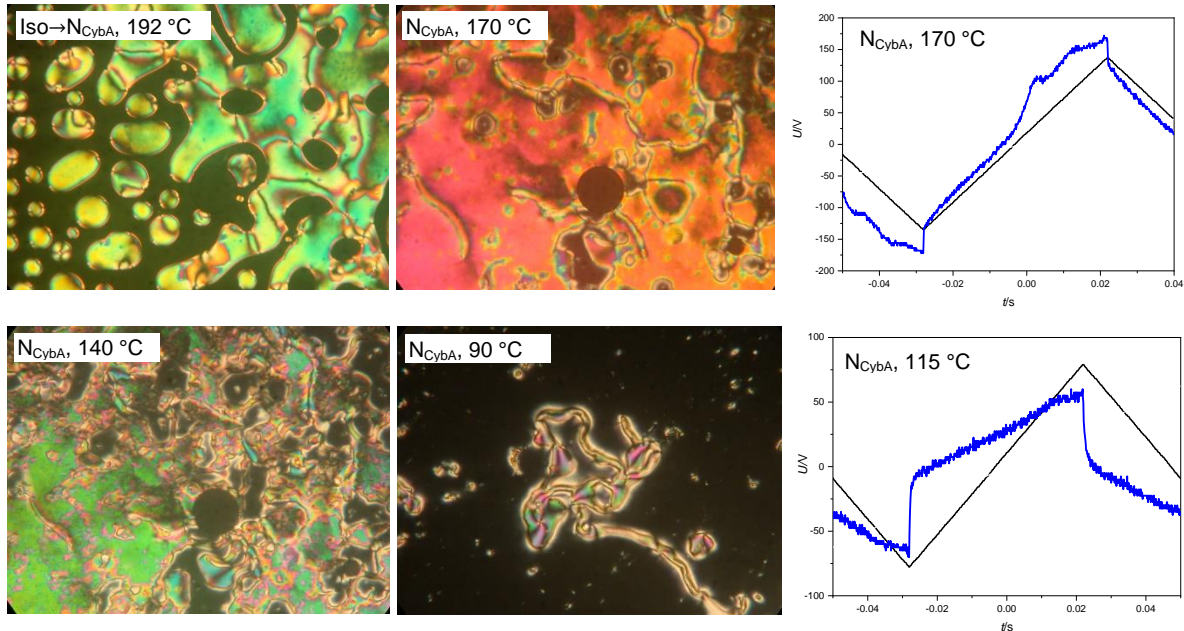


Figure S26. Textures of the nematic phase of **1/O2** depending on temperature as observed between crossed polarizers between ordinary microscopic glass plates; the dark areas at 192 °C are residues of the Iso phase, while at 90 °C the optically isotropic areas are due to homeotropic alignment of the sample, due to the growing size of the SmA-type cybotactic clusters. The switching current curves in 6 µm PI coated ITOO cells are shown at the right, the small broad features at 170 °C are most likely due to conductivity.

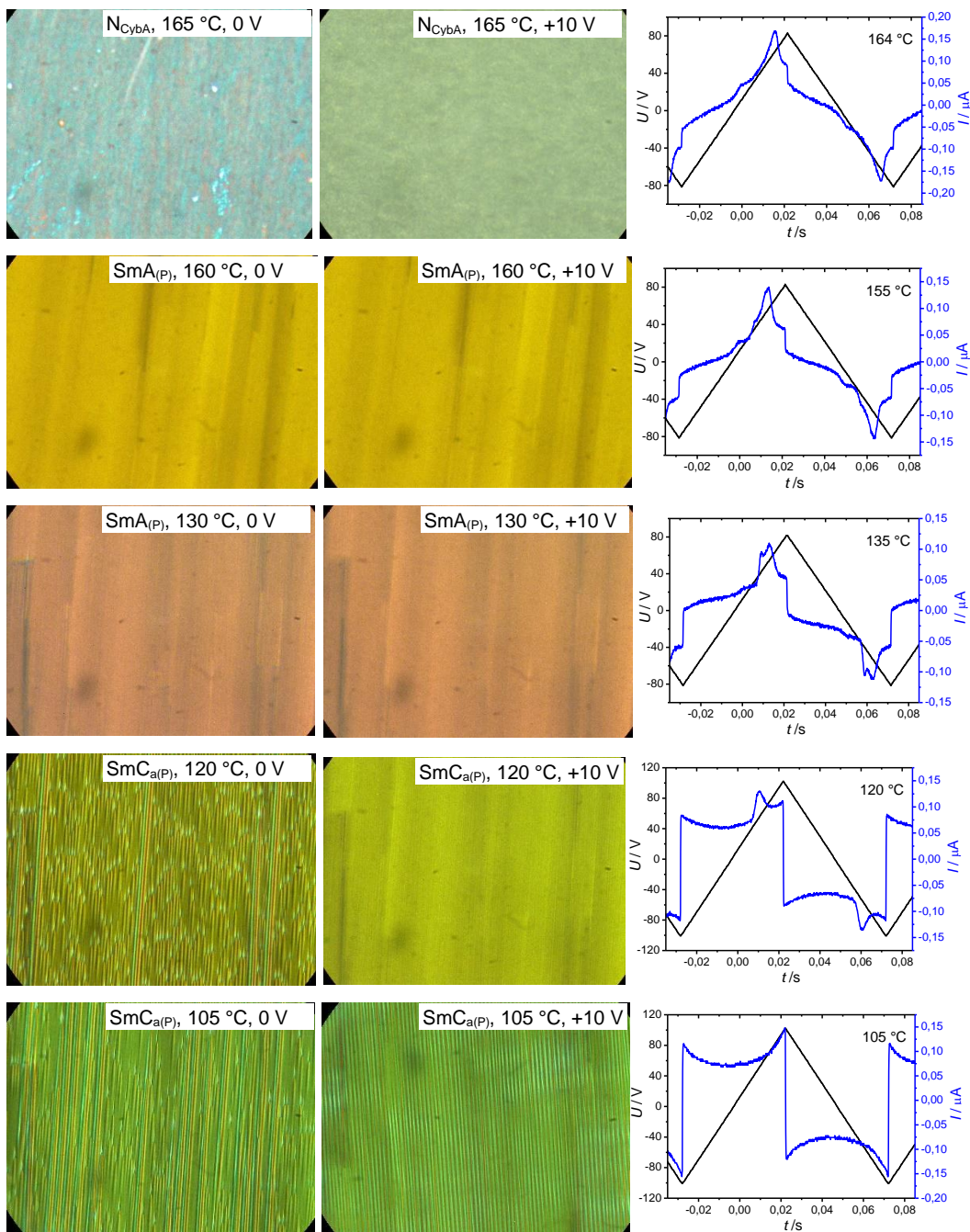


Figure S27. Textures of planar aligned samples of compound **1/O4** in a 6 μm PI-coated ITO cell and corresponding switching current curves under a triangular wave field (10 Hz, 160 V_{pp}). There is an optical response to the applied field in the nematic phase, this might be due to a change of the surface anchoring; no response or change of birefringence could be observed under an applied DC field in the SmA range, though in the nematic as well as in the SmA phase a broad peak can be observed in the current response curves. This peak is very small and is already observed in the Iso phase (175°C and higher) and could be due to a dielectric response or a conductivity. In the range of the SmC_a phase the peak disappears. The shape of the curves indicates that an antiferroelectric switching could possibly be achieved at higher applied voltages, but up to the maximum applied voltage of ± 200 V_{pp} no such switching can be observed. Therefore the LC phases are considered as non-polar, most likely paraelectric. There is an increase of birefringence in the SmA range due to the growing packing density; the decrease in birefringence from 130 to 120 °C is in line with the onset of a tilt.

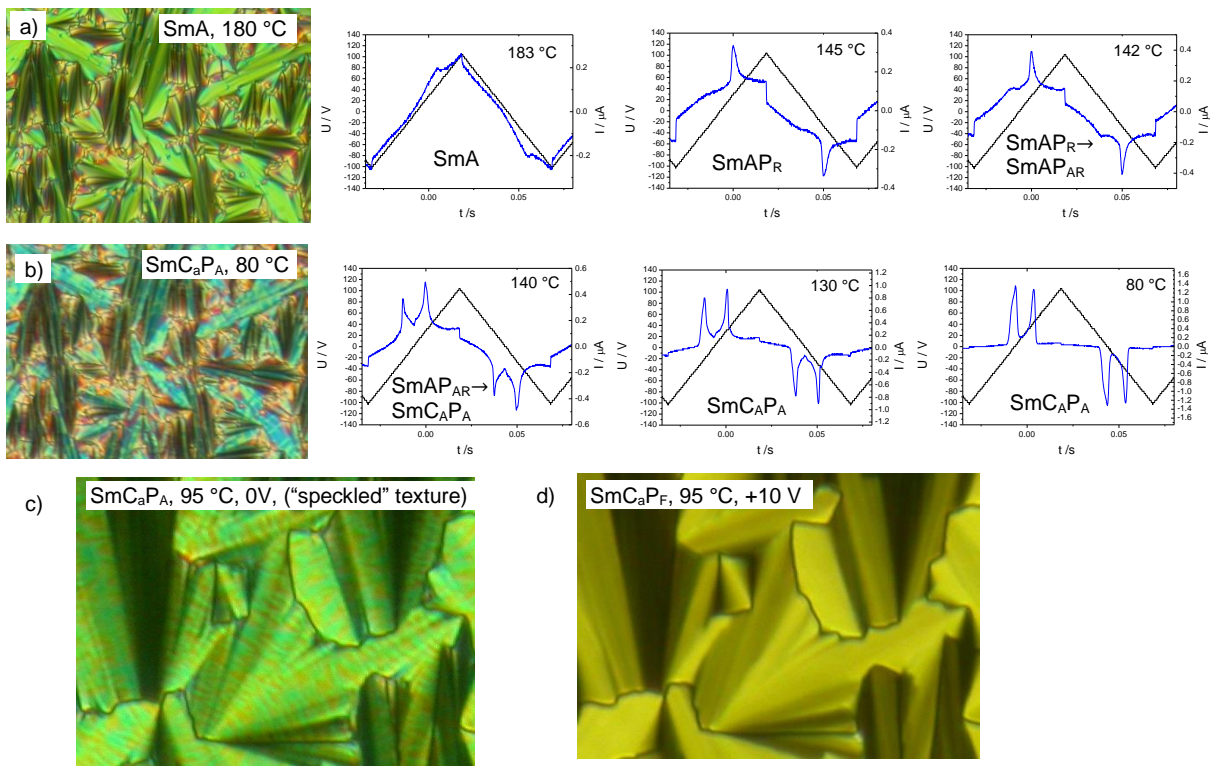


Figure S28. a, b) Textures and switching current curves of compound **1/O8** depending on temperature as measured in a in 6 μm PI-coated ITO cell; c) shows the typical “speckled” texture of the SmC_aPA phase of the 4-cyanoresorcinol compounds, which d) is removed in the field induced SmC_aPF state by collective rotation of the molecules around the long axis.

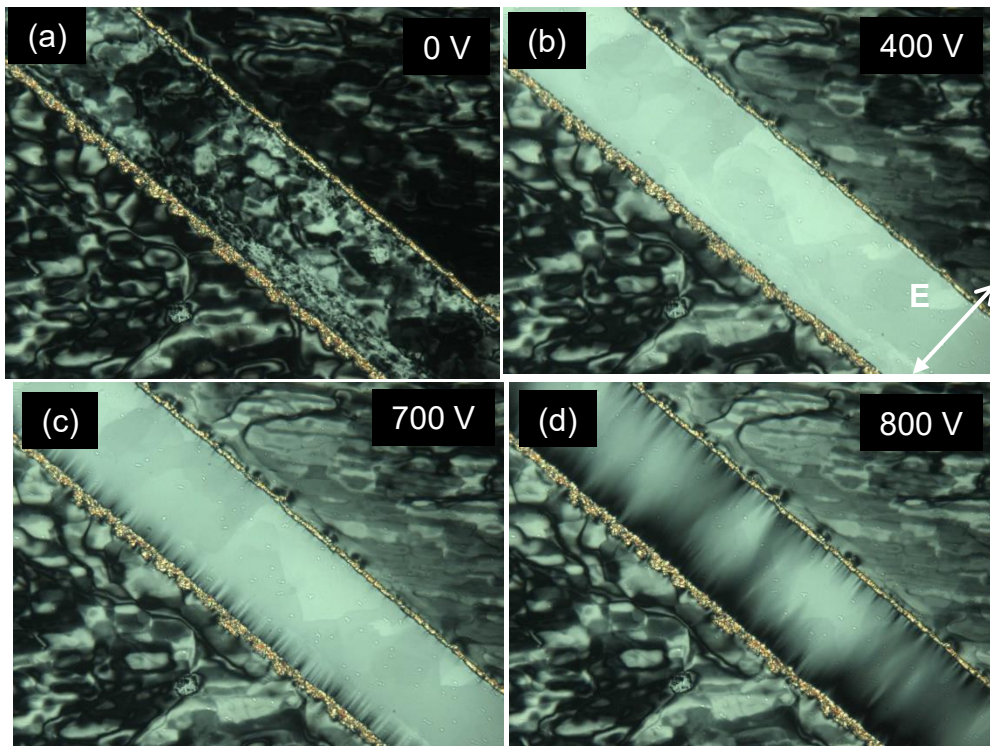


Figure S29. POM textures of **1/O10** in a homeotropic cell under an in-plane electric field at 127 °C, apparently no Sm(CP)^{hel} state can be induced with the maximal field applied; the distance between the electrodes is 180 μm .

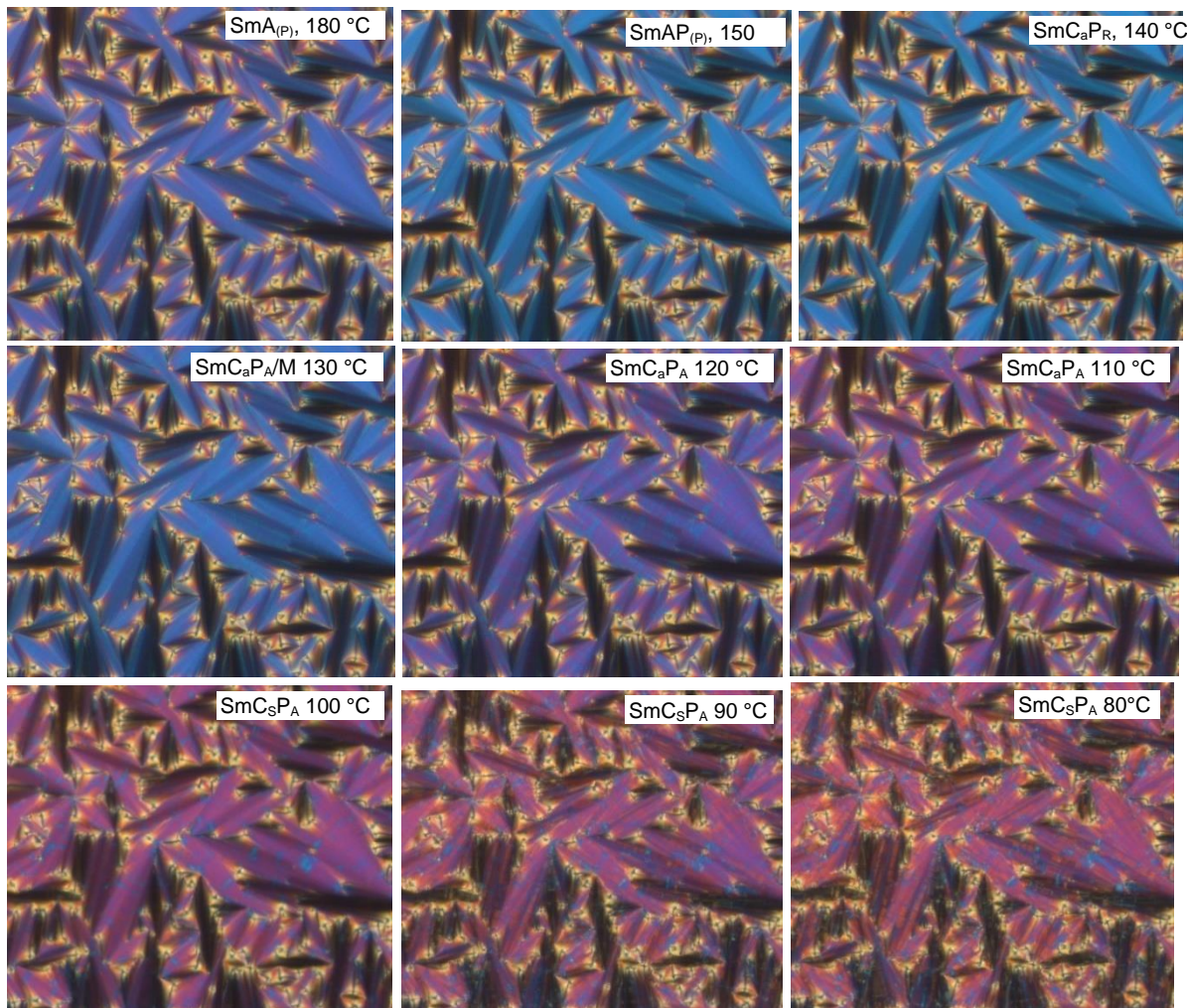


Figure S30. Textures of compound **1/O10** depending on temperature as measured in a in 6 μm PI-coated ITO cell at the indicated temperatures, as observed before application of any electric field.

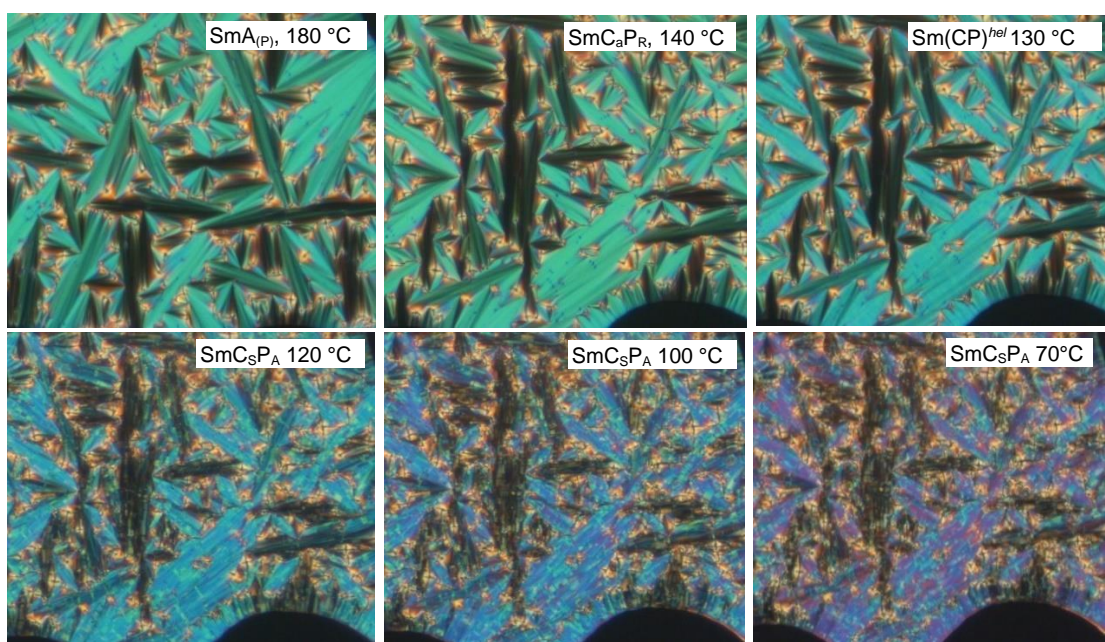


Figure S31. Textures of compound **1/O11** depending on temperature as measured in a in 6 μm PI-coated ITO cell at the indicated temperatures and observed before application of any electric field.

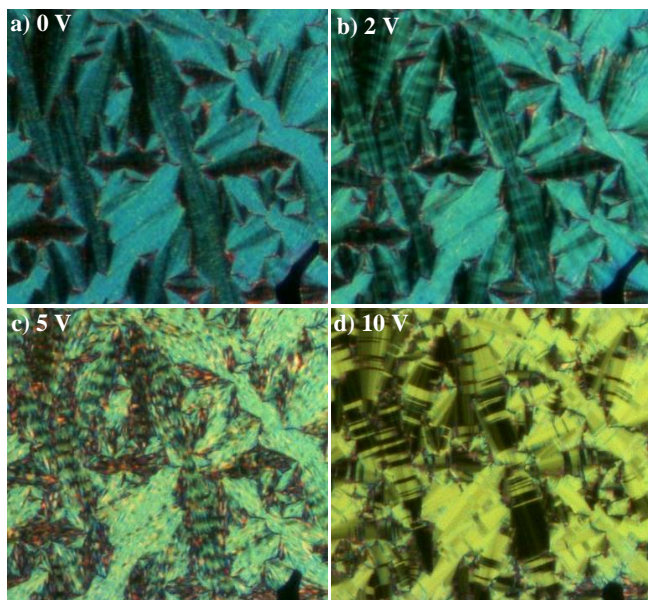


Figure S32a. Tiger stripes: Electrooptical investigation of the switching process of compound **1/O11** under an applied DC field in a 6 μm PI coated ITO cell in the $\text{SmC}_s\text{P}_F^{\text{hel}}$ range at $T = 128^\circ\text{C}$, showing the development of b, c) the “tiger stripe” texture changing into a d) tilt domain texture at highest voltage.

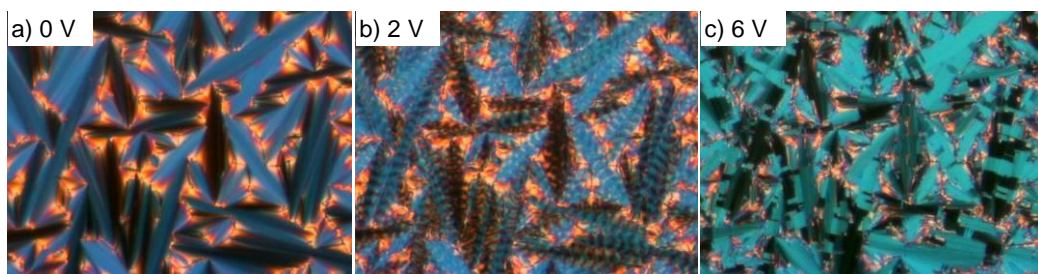


Figure S32b. Tiger stripes: Electrooptical investigations in the $\text{Sm}(\text{CP})^{\text{hel}}$ range of compound **1/O12** at $T = 130^\circ\text{C}$ in a PI coated ITO 6 μm planar cell under an applied DC field showing the development of the “tiger stripe” texture and the tilt domain texture at highest voltage.

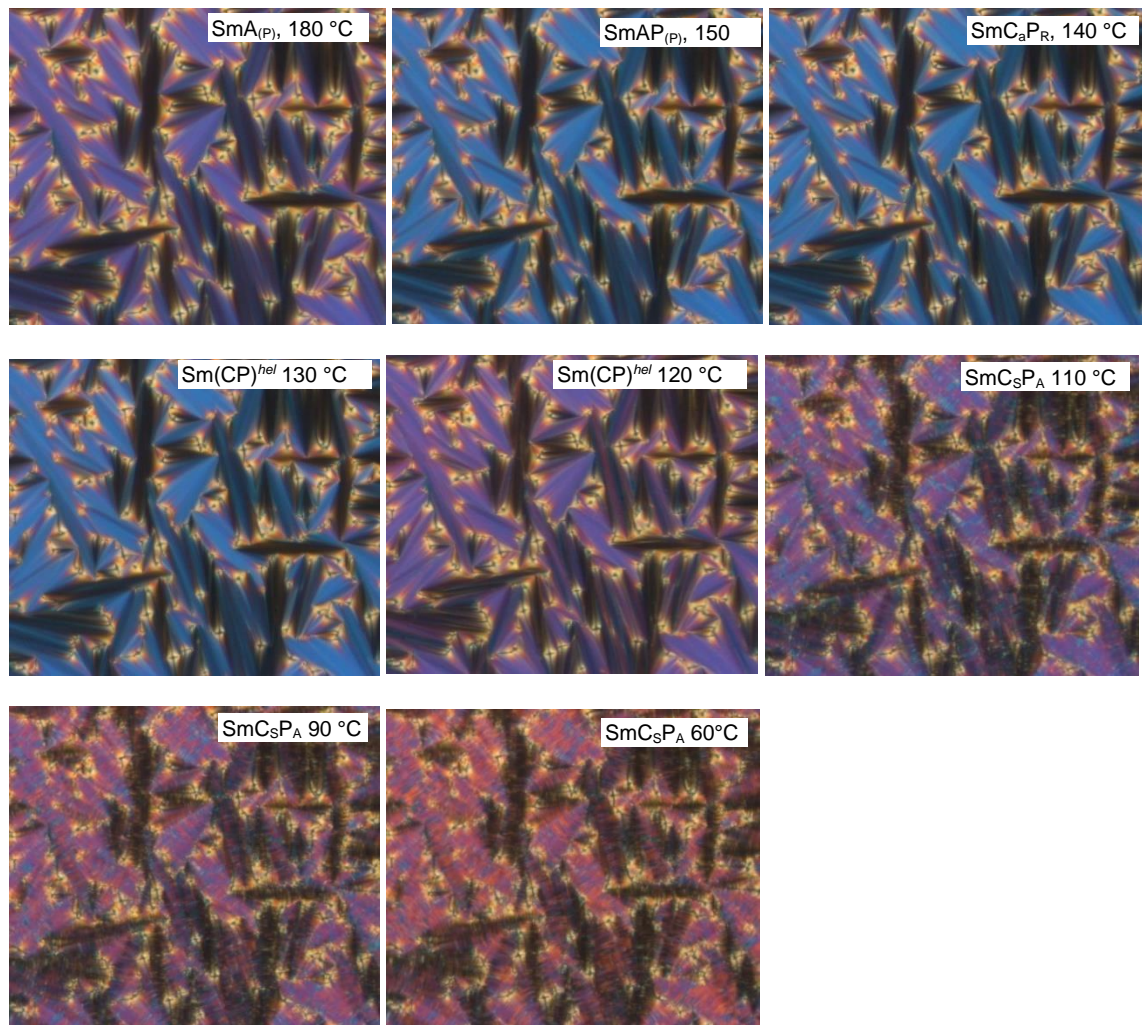


Figure S33. Textures of compound **1/O12** depending on temperature as measured in a in 6 μm PI-coated ITO cell at the indicated temperatures, as observed before application of any electric field.

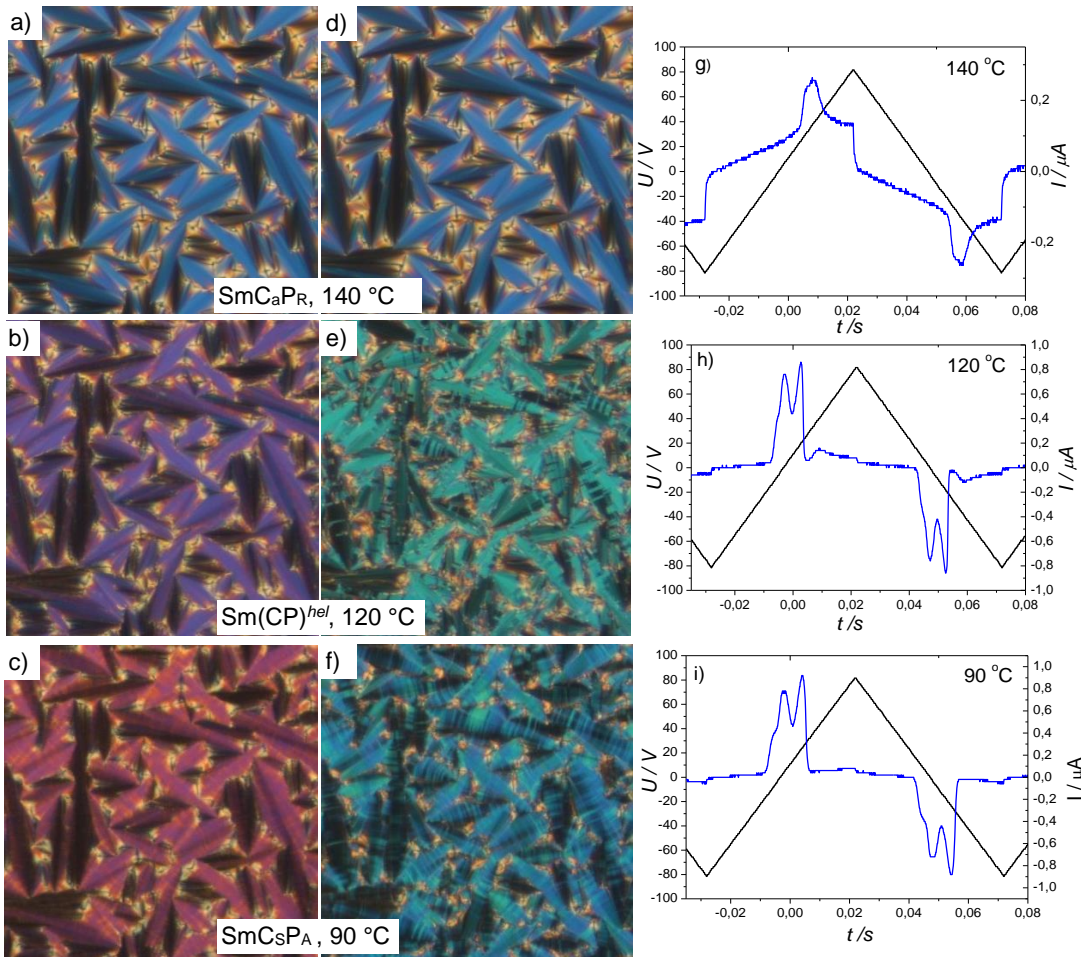


Figure S34. Optical micrographs of the textures observed for the different LC phases of compound **1/O12** in a PI coated ITO 6 μm planar cell without electric field (a-c left column), under an applied DC field (d-f right column) and polarization current response curves (h-i) at the indicated temperatures for the indicated LC phases.

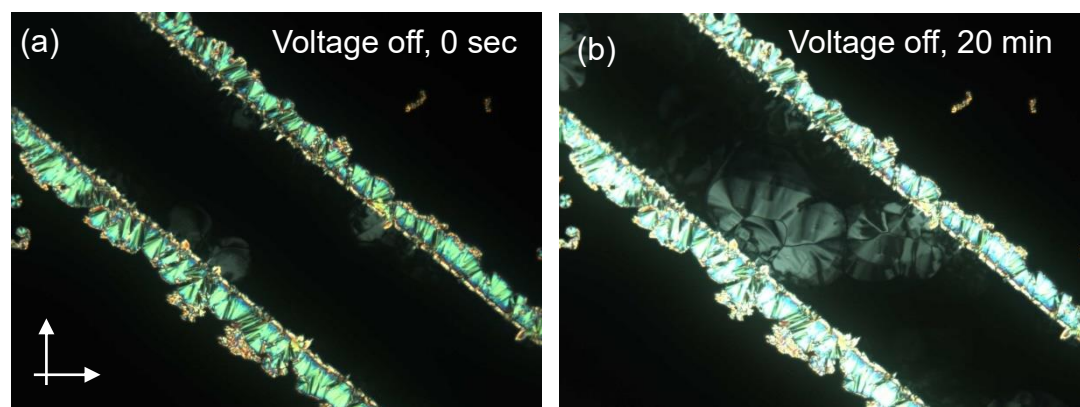


Figure S35. POM textures of **1/O12** after turning off the voltage after the helix is induced in a homeotropic cell on application of an in-plane electric field at 127 °C; the birefringent fans have the extinctions inclined with respect to the polarizers, thus indicating the relaxation to a SmCsPA structure. This indicates that the Sm(CP)^{hel} phase is metastable in this case. The gap between the electrodes is 180 μm.

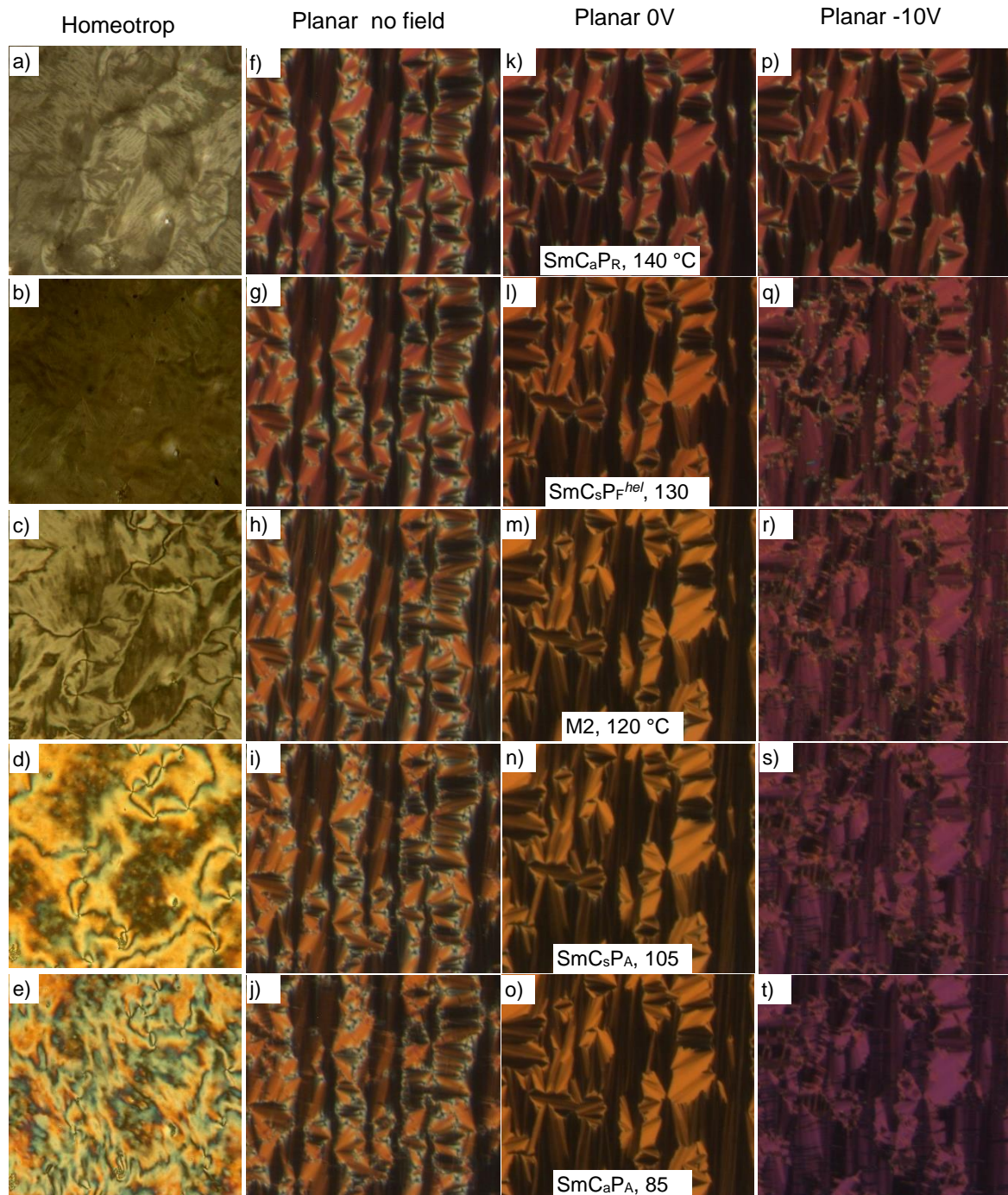


Figure S36. Optical micrographs of the textures observed for the different LC phases of compound **1/O14** in homeotropic cell (a-e); in a PI coated ITO 6 μm planar cell without electric field (f-j), after applying 10 V DC field and removing it (k-o) and under 10 V DC field (p-t) at the indicated temperatures for the indicated LC phases.

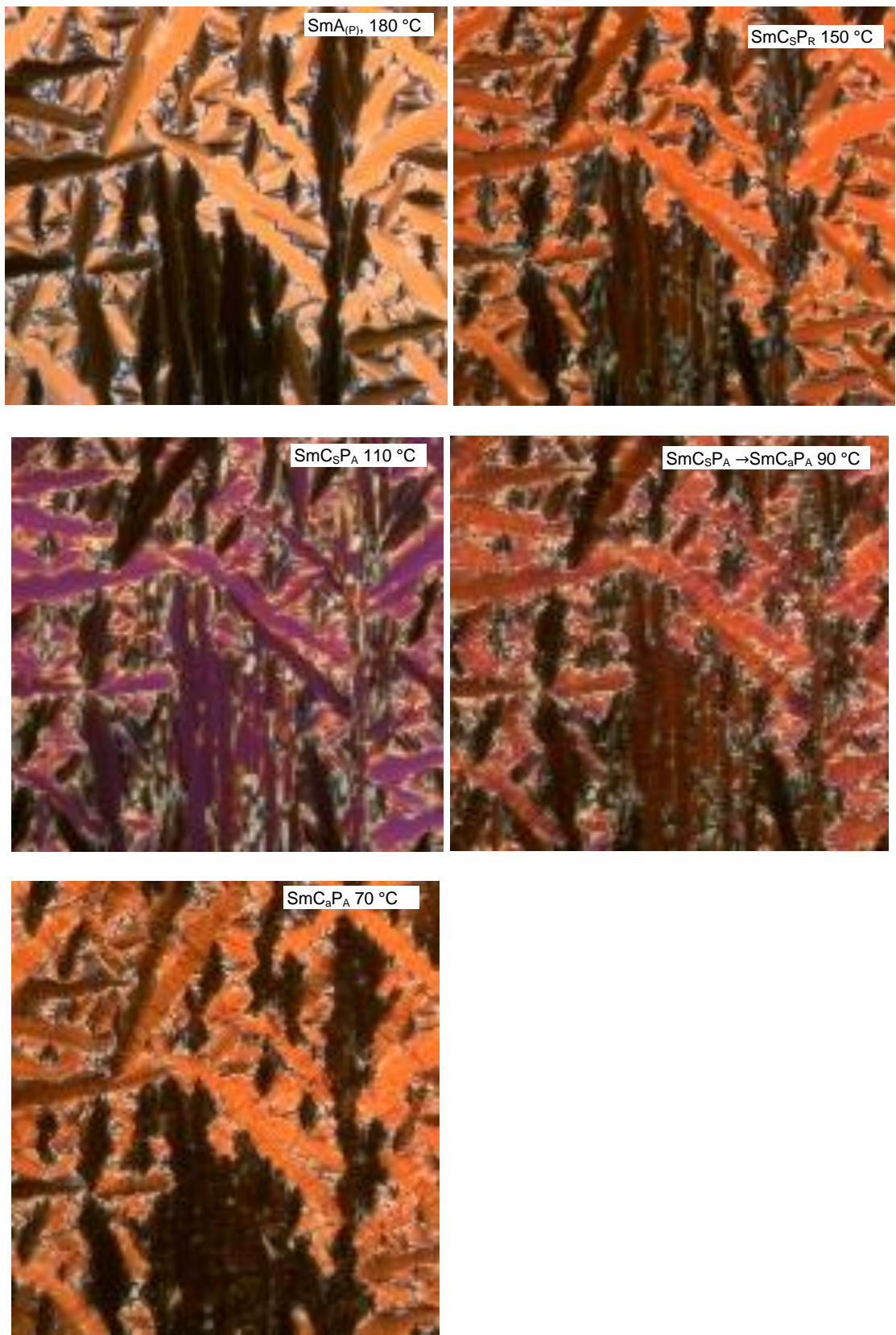


Figure S37. Textures of compound **1/O16** depending on temperature as measured in a in $6\text{ }\mu\text{m}$ PI-coated ITO cell at the indicated temperatures, as observed before application of any electric field.

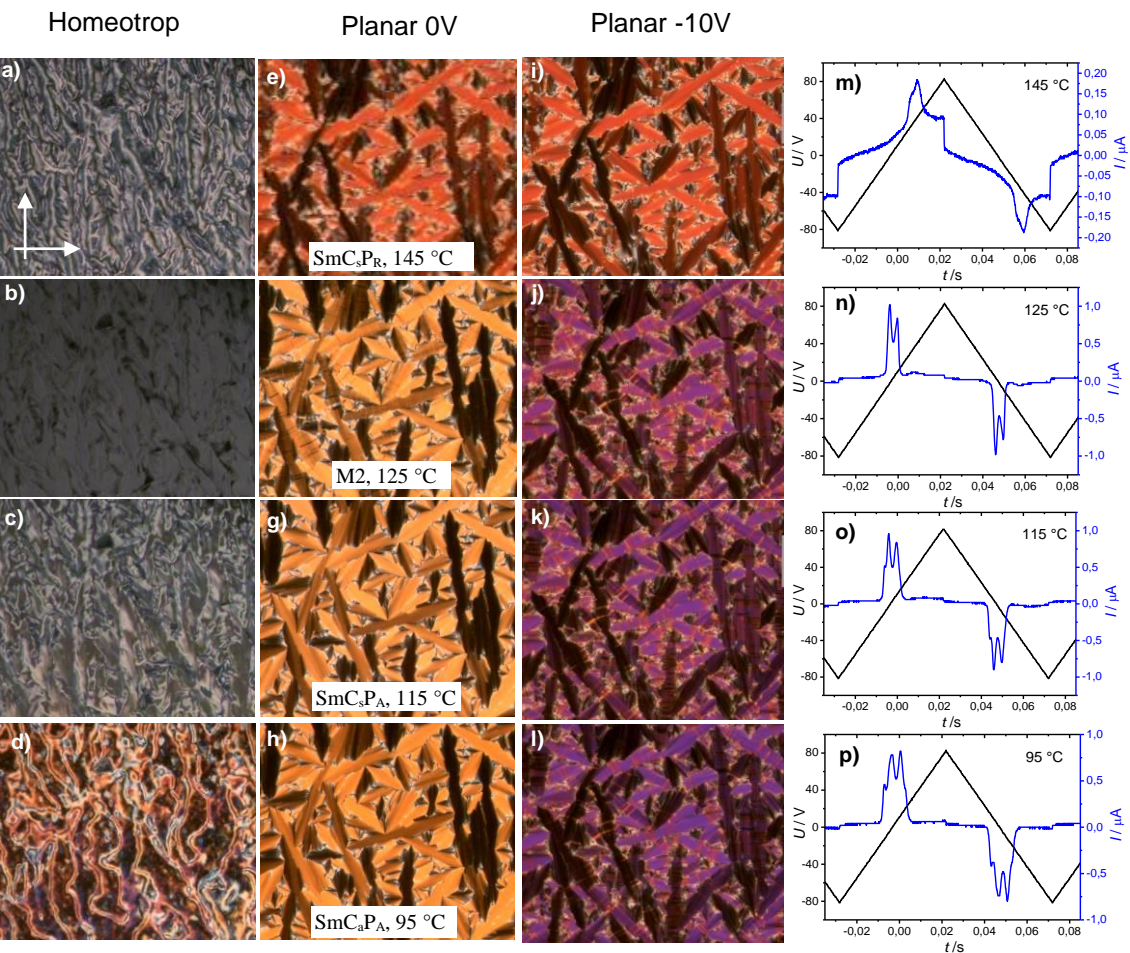


Figure S38. Optical micrographs of the textures observed for the different LC phases of compound **1/O16** in a homeotropic cell (left column) and in a PI coated ITO 6 μm planar cell without EF (middle column), after applying 6V DC field and polarization current response curves in the same cell (right column) at the indicated temperatures for the indicated LC phases.

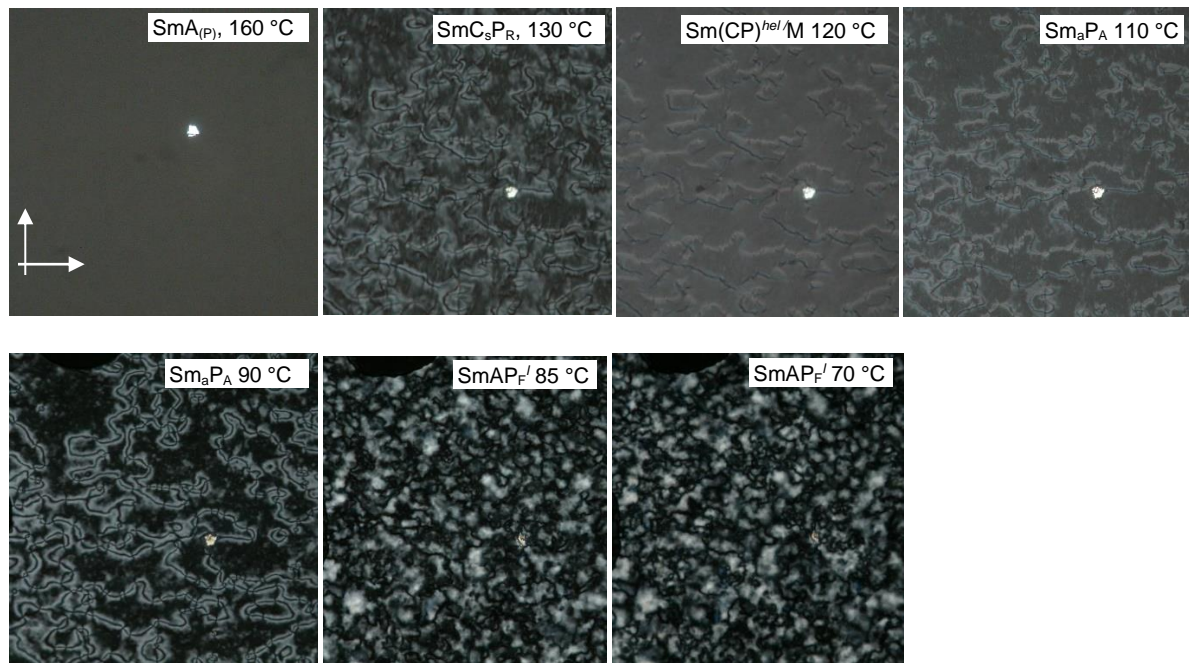


Figure S39. Homeotropic textures of compound **1/O18** at the indicated temperatures, as observed before application of any electric field.

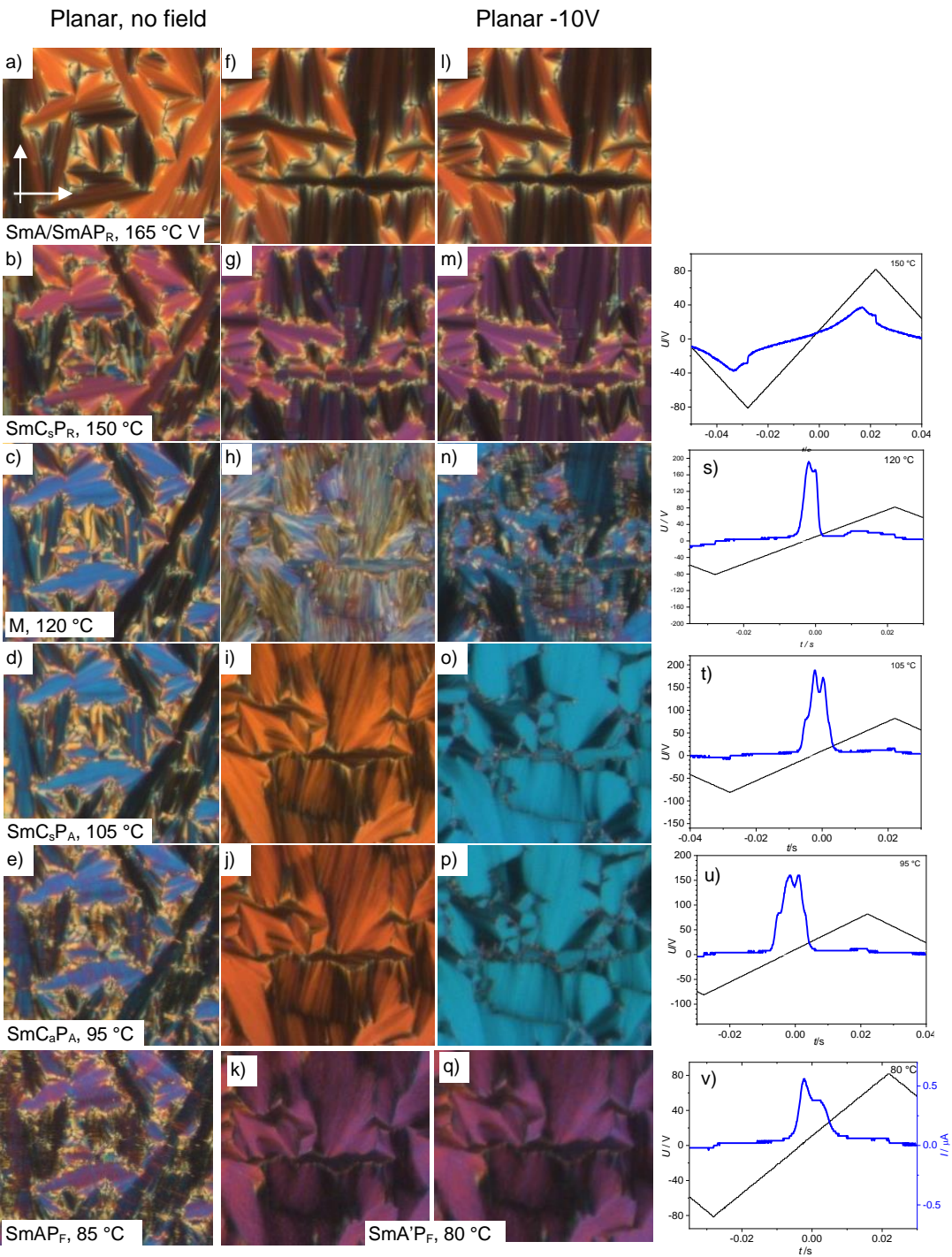


Figure S40. Optical micrographs of the textures observed for the different LC phases of compound **1/O18** in a PI coated ITO 6 μ m planar cell (a-e) without electric field, after applying 10 V DC field and removing it (f-j) and under 10 V DC field (k-o) for the LC phases at the indicated temperatures.

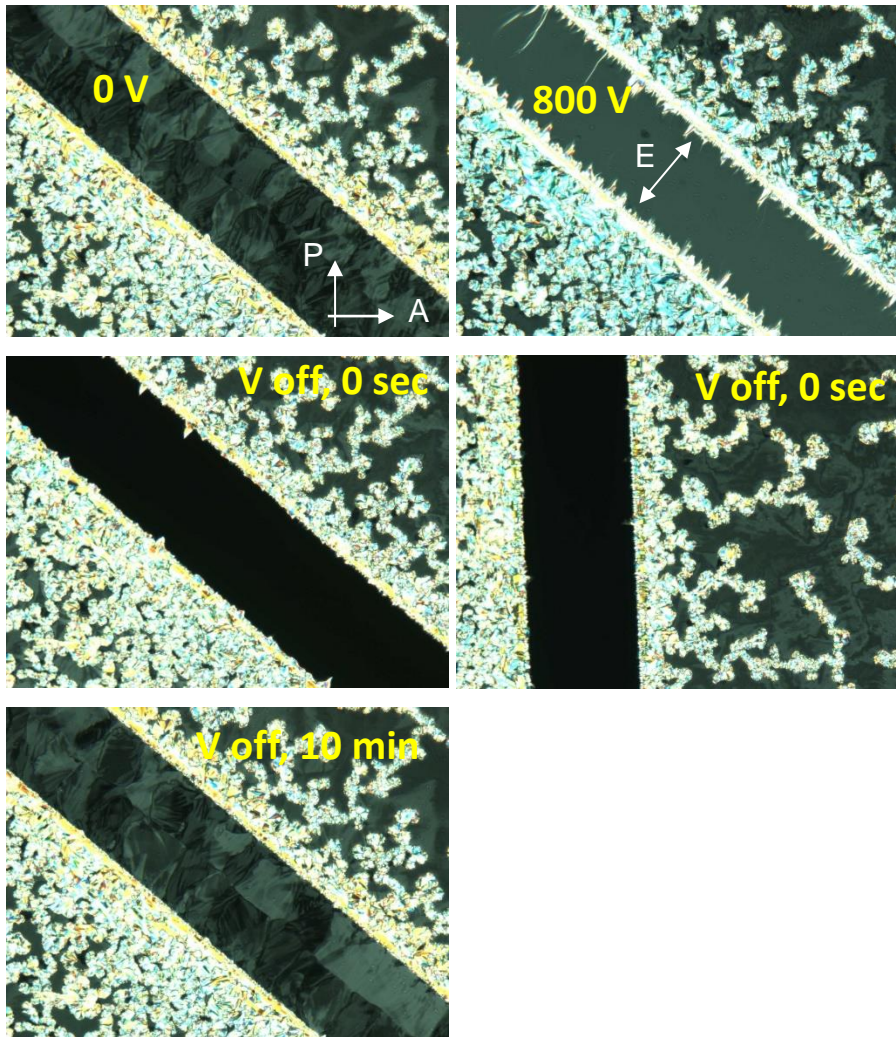


Figure S41. POM textures in a 9 μm homeotropic cell filled with **1/O18** under in-plane electric field applied at $T = 120$ $^{\circ}\text{C}$ in the SmCsPA phase at 110 Hz. The field induced optical pseudo-isotropic area between the electrodes indicates the uniaxiality due to the development of a short-pitch heliconical structure in the field-induced $\text{Sm}(\text{CP})^{\text{hel}}$ state. There is a slow relaxation to the SmCsPA state after the applied field is switching off. The gap between the electrodes is 180 μm .

6. Identification and confirmation of heliconical phases

Conventional chiroptical methods like optical rotation measurements and CD are not applicable for indicating helicity/chirality in birefringent LC phases, because the effects of birefringence are much larger than the effects of optical rotation. In addition, the helix pitch in the $\text{Sm}(\text{CP})^{\text{hel}}$ phases is too short (3-4 molecules) to be directly identified by optical methods. Moreover, even in (optical isotropic) homeotropic alignment, no typical conglomerate textures, as for example known for the optical isotropic dark conglomerate phases (DC) and helical nanofilament phases (HNF) can be observed for **1/n**, **1/On** and related compounds by POM between polarizers being slightly (+/- 1-5°) uncrossed from exactly 90°. The reason might be that in heliconical smectic phases the major twist takes place between the layers which are separated by alkyl chain layers, which separate the π -systems of neighboring layers. Moreover, the twist between the main conjugation pathways of neighboring π -systems within the layers is much smaller. Both effects

lead to an only small exciton coupling between the π -systems of the molecules, which is mainly responsible for optical rotation in supramolecular helical systems.[S8] Moreover, achieving homeotropic alignment requires thin samples (10-20 μm) providing only small values of optical rotation which cannot be recognized in such thin samples by conglomerate formation observable by POM between slightly uncrossed polarizers. Often additional surface treatment and shearing are required for homeotropic alignment which can in addition distort the development of sufficiently large uniformly chiral domains.

Nevertheless, the helical superstructure of compound **1/14**, as an example, was unambiguously proven by soft resonant X-ray scattering at the ^{13}C -edge, which circumferences these limitations, though it is not a routine method.[S9] However, from these investigations the typical features of these heliconical phases (ground state structures and induced structures after application of a short AC sequence) were identified, allowing the indirect confirmation of helix formation of other bent-core compounds based on a combination of optical (POM) and electrooptical studies. The main criteria are the following:

1. In homeotropic alignment the $\text{Sm}(\text{CP})^{\text{hel}}$ phases appear optically isotropic, despite of a proven tilted and/or long range polar (“ferro- or antiferroelectric”) organization of the molecules in smectic phases (see Fig. 10c). In this case the uniaxiality is due to the short pitch helix.
2. In planar alignment with fan-like/spherulitic textures the dark extinctions appear parallel to polarizer and analyzer as in SmA, SmAP_A, SmAP_R and SmC_aP_A phases, despite of the presence of an otherwise proven (almost) synclinic tilt (Fig. 10g-j).
3. Under an applied DC-field with increasing strength (applied between the cell surfaces) a regular pattern of alternating dark and bright stripes on the birefringent fans (tiger stripe pattern) is induced perpendicular to the fan direction due to partial helix unwinding (see Fig. 10f). This tiger stripe texture is observed for a distinct (compound specific) field strength and is replaced by the usual chiral domain texture of the field induced SmCsPF states.
4. In homeotropic alignment helix unwinding is indicated by induction of birefringence under an increasing applied in-plane E-field. On the other hand, a field induced helix can be indicated by a decreasing birefringence and formation of an optical isotropic state upon application of an in-plane E-field (see Fig. 11).
5. Under an applied triangular wave AC field three current response peaks with the two peaks at lower voltage being close side-by side (often only recognized as a shoulder or a significantly broadened peak) supports the identification of a heliconical superstructure with commensurate or incommensurate 3-layer periodicity (see Fig. 10r).
6. Field-induced formation of the heliconical phase from SmCsPA after application of a short AC sequence is associated with a change of the orientation of the dark extinctions from being inclined to parallel with respect to the crossed polarizers, combined with a reduced birefringence in the birefringent fans/spherulites (see Fig. 13q-s). Though this texture is also found for SmAP_{A/F} and SmCaPA phases with an alignment of the molecules with the bow plane parallel to the surface, in these cases the extinctions remain parallel to the polarizers under an applied field,[S10] while from the $\text{Sm}(\text{CP})^{\text{hel}}$ phase the extinctions become inclined under the applied field due to the transition to SmCsPF.

7. Additional SHG and dielectric data

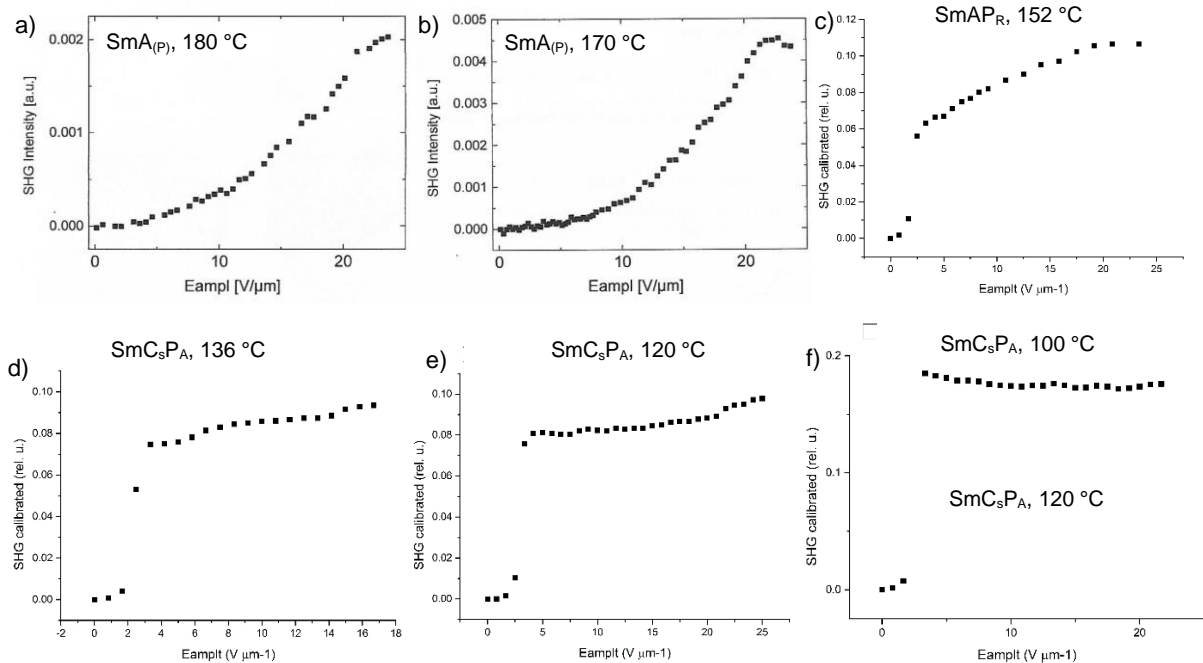


Figure S42: Field dependence of SHG activity of 1/O10 depending on the temperature.

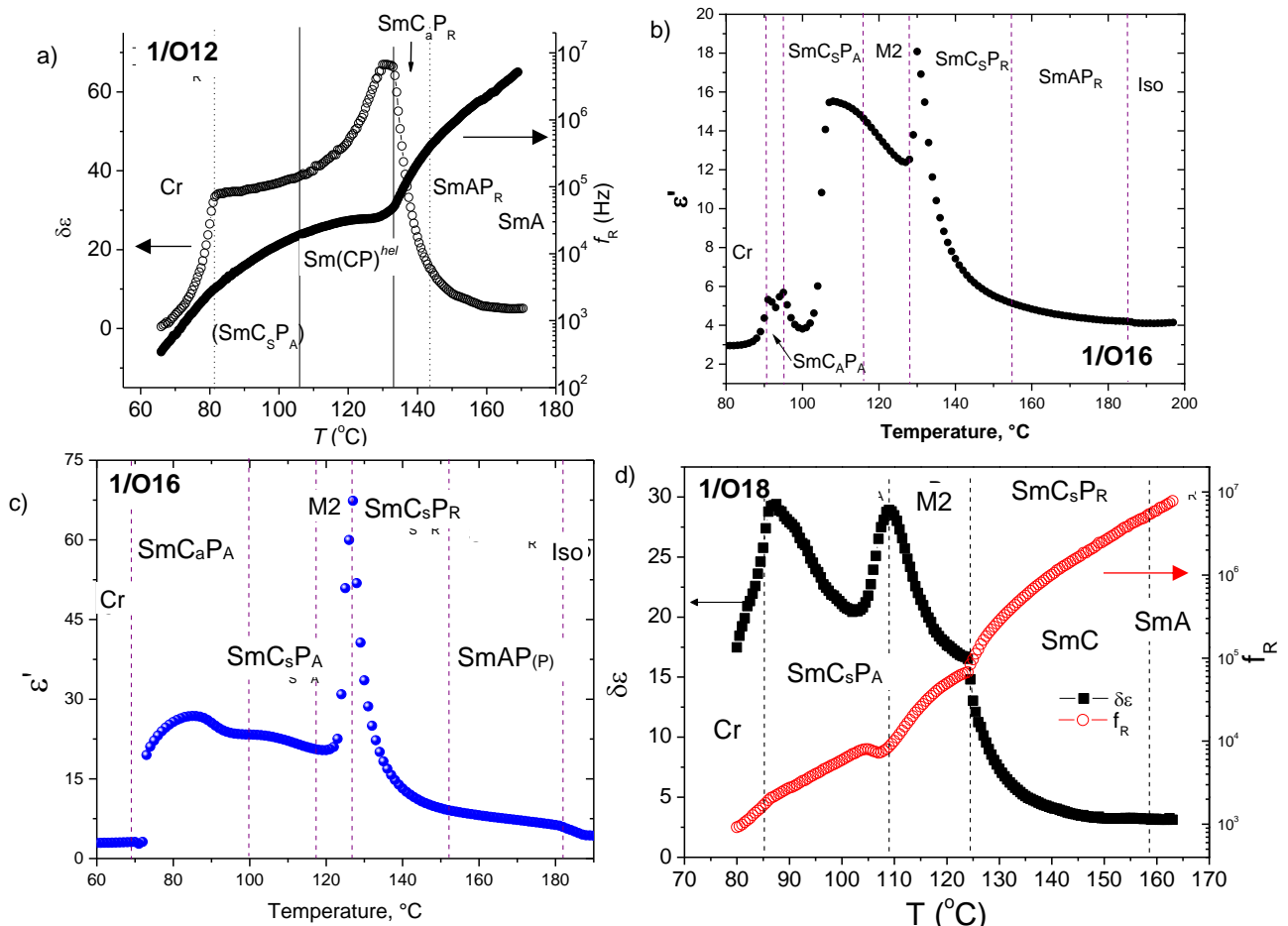


Figure S43. a) Dielectric permittivity of various LC phases depending on temperature. a) 1/O12 on cooling, b) 1/O16 on cooling and c) 1/O16 on heating and d) 1/O18 (planar aligned cell 30 μm, frequency 1 kHz).

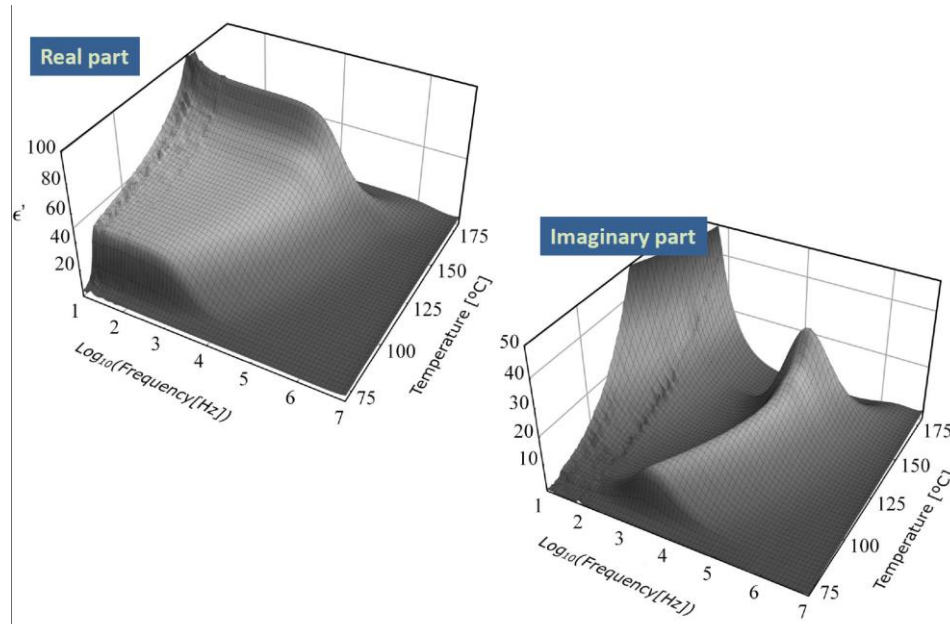


Figure S44: a) Real and imaginary part of permittivity versus frequency and temperature for compound **1/O10**.

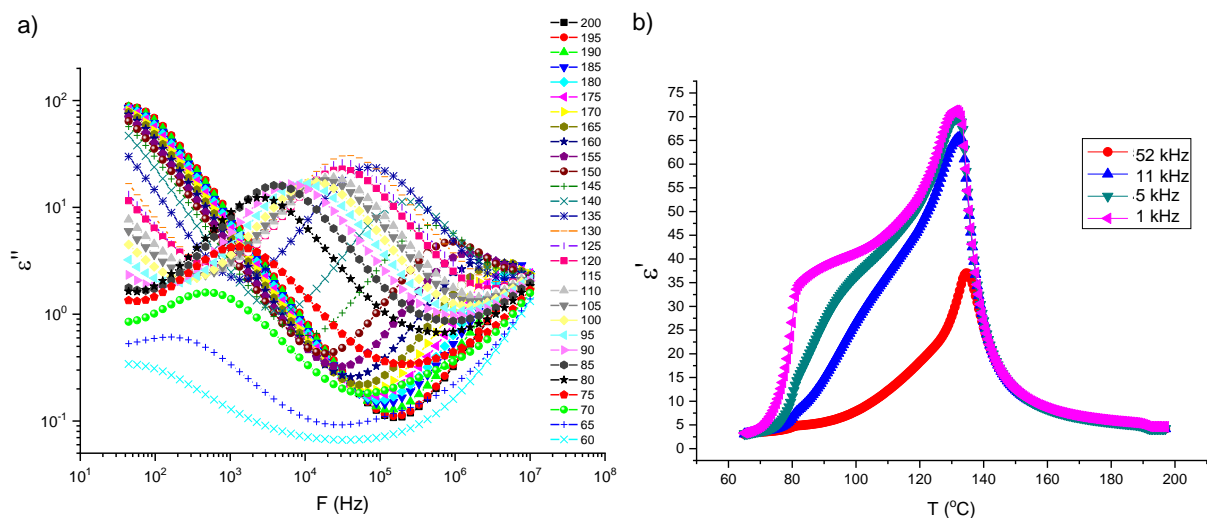


Figure S45: a) The imaginary part of permittivity (ϵ'') versus frequency at different temperatures (°C) and b) the real part of permittivity versus temperature for different frequencies (in Hz) for compound **1/O12**.

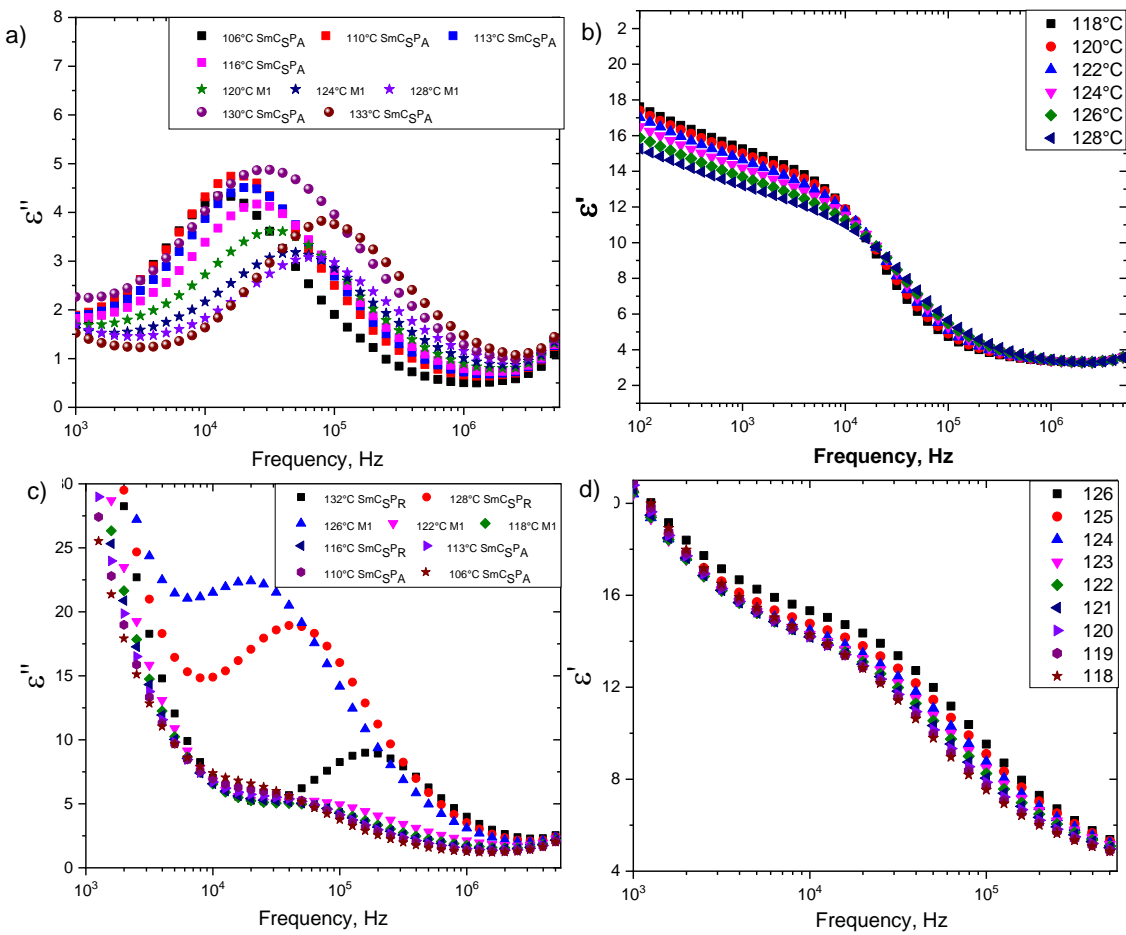


Figure S46. a, c) The imaginary part of dielectric permittivity (ϵ'') vs. Frequency at different temperatures 30 μm Planar cell b, d) the real part of dielectric permittivity (ϵ') vs. frequency for various temperatures of compound **1/O18**, a b) measured on heating and c, d) measured on cooling (30 μm planar aligned cell).

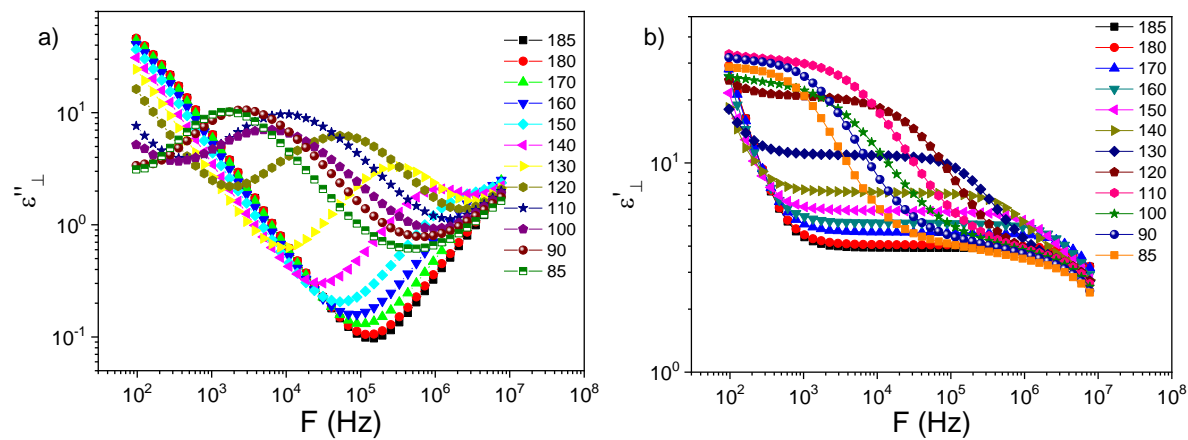


Figure S47. a) The imaginary part of dielectric permittivity (ϵ'') vs. Frequency at different temperatures 8 μm Planar cell b) The real part of dielectric permittivity (ϵ') vs. Frequency for various temperatures of compound **1/O18**.

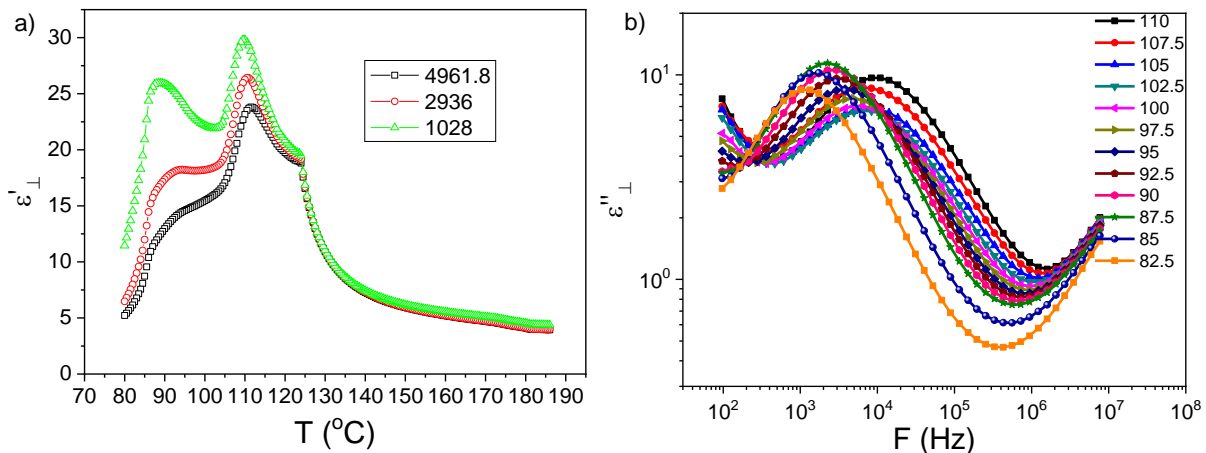


Figure S48. The real part of dielectric permittivity (ϵ') vs Temperature for selected frequencies (in Hz) The imaginary part of dielectric permittivity (ϵ'') vs Frequency for selected temperatures of compound **1/O18**.

8. Additional Investigation of freely suspended films

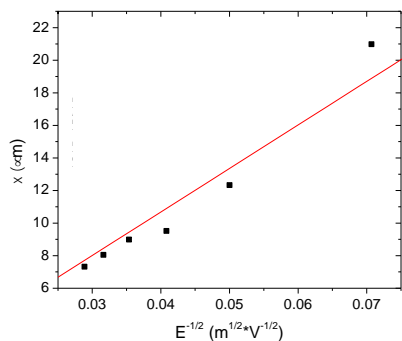


Figure S49. Inversion wall thickness as a function of an electric field applied to an $1.9 \mu\text{m}$ thick freely suspended film in the SmC_aP_R phase of **1/O10** at $T=145^\circ\text{C}$.

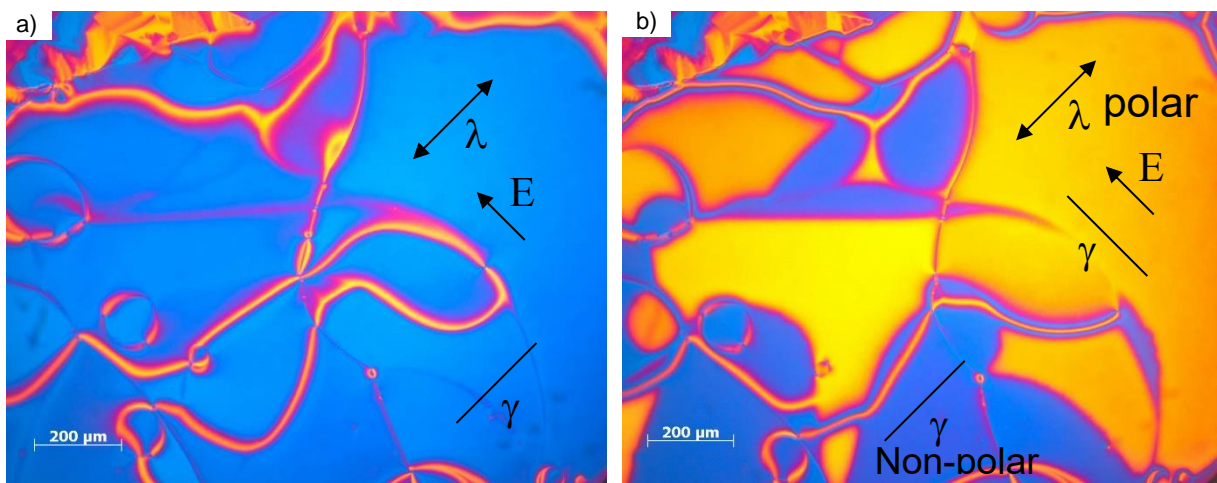


Figure S50. Freely suspended film (750 nm) of **1/O10** at 136°C on cooling at the SmC_SP_R - SmC_SP_A transition. The yellow domains are the polar domains, where the easy axis γ aligns along the electric field E (1V DC). The easy axis γ is perpendicular to the λ plate; In the blue domains, the non-polar (dielectric) domains, the easy axis γ aligns perpendicular to the applied electric field. The easy axis γ is parallel to the λ plate

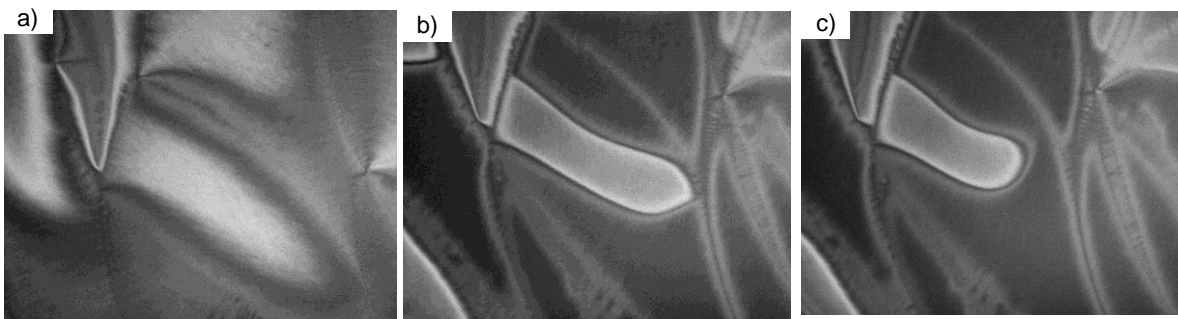


Figure S51. Polarising microscopy images of 2.3 μm thick freely suspended film of **1/O20** in the SmCP_R phase at 143 °C in a) the field-free state, and in an electric field b) -69 V/mm, c) +69 V/mm. Thin (π) director inversion walls and identical states for opposite polarities confirm that the phase does not have a spontaneous polarization; the image width is 700 μm .

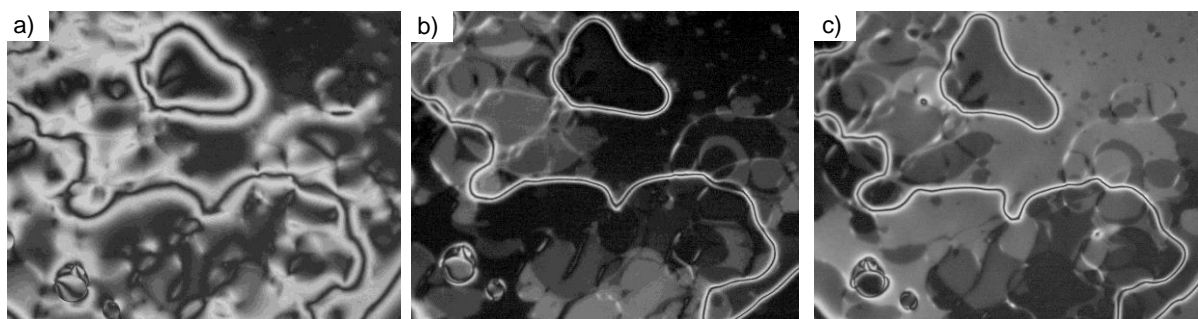


Figure S52. Polarising microscopy images of 4.2 μm thick freely suspended film of **1/O20** in the SmCaPA phase at 94 °C in a) the field-free state, and in an electric field b) -69 V/mm, c) +69 V/mm. Thin (π) director inversion walls confirm that the phase does not have a spontaneous polarization; the image width is 700 μm .

9. References

- S1. I. Wirth, S. Diele, A. Eremin, G. Pelzl, S. Grande, L. Kovalenko, N. Pancenko and W. Weissflog, *J. Mater. Chem.*, 2001, **11**, 1642.
- S2. a) M. Alaasar, M. Prehm, M. Poppe, M. Nagaraj, J. K. Vij, C. Tschierske, *Soft Matter.*, 2014, **10**, 5003; b) N. Sebastian, S. Belau, A. Eremin, M. Alaasar, M. Prehm, C. Tschierske, *Phys. Chem. Chem. Phys.*, 2017, **19**, 5895.
- S3. W.-S. Bae, J.-W. Lee, J.-I Jin, *Liq. Cryst.*, 2001, **28**, 59.
- S4. J.-I. Jin, H.-S. Kim, J.-W. Shin, B. Y. Chung, B.-W. Jo, *Bull. Kor. Chem. Soc.*, 1990, **11**, 209.
- S5. a) V. Kozmík, M. Horcic, J. Svoboda, V. Novotna, D. Pociecha, *Liq. Cryst.*, 2012, **39**, 943; b) S. Kapuscinski, A. Wojciechowska, K. Urbaniak, P. Kaszynski, M. Jasinski, *Liq. Cryst.*, 2017, **44**, 1093.
- S6. a) K. Pelz, S. Findeisen, G. Pelzl, S. Diele, W. Weissflog, *Liq. Cryst.*, 2006, **33**, 803; b) G. Pelzl, H. N. S. Murthy, M. W. Schröder, S. Diele, Z. Vakhovskaya, H. Kresse, W. Weissflog, *J. Mater. Chem.*, 2006, **16**, 1702.
- S7. M. Alaasar, M. Prehm, C. Tschierske, *Chem. E. Jur.*, 2016, **22**, 6583.
- S8. G. Pescitelli, L. Di Bari, N. Berova, *Chem. Soc. Rev.* 2014, **43**, 5211.

-
- S9. A. A. S. Green, M. R. Tuchband, R. Shao, Y. Shen, R. Visvanathan, A. E. Duncan, A. Lehmann, C. Tschierske, E. D. Carlson, E. Guzman, M. Kolber, D. M. Walba, C. S. Park, M. A. Glaser, J. E. MacLennan and N. A. Clark, *Phys. Rev. Lett.* 2019, **122**, 107801.
- S10. A. Lehmann, M. Alaasar, M. Poppe, S. Poppe, M. Prehm, M. Nagaraj, S. P. Sreenilayam, Y. P. Panarin, J. K. Vij and C. Tschierske, *Chem. Eur. J.* 2020, **26**, 4714 (Figs. 16, 19).